

Rayleigh Wave Acoustic Emission during Crack Propagation in Steel

Michael R. Horne

Dissertation submitted to Faculty of the
Virginia Polytechnic Institute and State University
in partial fulfillment of the requirements for the degree of

Doctor of Philosophy
in
Materials Engineering Science (MESE)

Dr. J. C. Duke, Jr., Chairman
Dr. N. E. Dowling
Dr. D. P. H. Hasselman
Dr. E. G. Henneke
Dr. W. T. Reynolds, Jr.

August 1, 2003
Blacksburg, VA

Keywords: NDE, Stress Wave Propagation, Fatigue
Copyright 2003, Michael R. Horne

Rayleigh Wave Acoustic Emission during Crack Propagation in Steel

Michael R. Horne

(ABSTRACT)

An investigation was conducted of the existence of seismic surface pulses (SSP) on crack faces in near-failure fatigue. An SSP has components of various modes of wave propagation. The component with the largest amplitude is a Rayleigh surface wave pulse. The possibility that these surface modes have much higher amplitudes than bulk modes of acoustic emission (AE) was illustrated by an idealized thought experiment relating an SSP on a half-space to the response of crack faces to crack extension.

A number of aspects of AE monitoring in finite objects were investigated. Attributes of surface wave propagation on the edge of a specimen were found to be easier to monitor than other modes of wave propagation. Wavelet analysis was used to compare the characteristics of brittle AE with other sources.

A new testing paradigm was developed to reduce interference from secondary sources of AE and enhance the investigation of AE from critical crack behavior. Unique specimen design features were developed, data acquisition features sought and validated, a dead weight load frame was modified, and data analysis procedures were developed. Criteria based on velocity, frequency content, amplitude and shape were devised to determine if an AE event is an SSP. The tests were designed to mimic load conditions on structures such as bridges and hence investigate the difference between AE generated in field conditions and that of typical laboratory conditions. Varieties of steel, from very ductile to very brittle, were tested.

It was concluded that plastic zone formation, considered a secondary source of AE, was found not to interfere with the SSP activity. The SSP was found experimentally to have 2-3 times the amplitude of the bulk wave AE. The lack of sufficient AE did not allow for determination of conclusive changes in the AE as the specimens approached failure. However, it was found that brittle crack extension in fatigue and ductile failure can produce wave propagation resembling the SSP.

Acknowledgments

The bulk of this effort was conducted during a research program "Quality Assurance Testing of High Performance Steel Bridge in VA" (98-1687-04) for the Virginia Transportation Research Council. Acknowledgment should also be made to Vallen-Systeme GmbH for providing to the research community, free, the wavelet analysis software used in this research.

I would also like to thank my family, my supervisor and committee chair, my committee (including Dr. R. G. Kander who was unable to be on my examining committee), and many others for their help and patience during this journey.

Contents

Preface

1	Introduction	1
1.1	The Problem of Crack Propagation	2
1.2	Possible NDT to Measure Crack Extension	3
1.2.1	Acoustic Microscopy	3
1.2.2	Ultrasonic Tip Diffraction	3
1.2.3	Potential Drop	3
1.2.4	Compliance	4
1.2.5	Acoustic Emission	4
1.2.6	Summary	6
1.3	Measuring Criticality Directly	7
2	Theoretical Considerations	10
2.1	Wave Propagation.....	10
2.1.1	Rayleigh Waves and the Seismic Surface Pulse.....	10
2.1.2	Edge Waves.....	11
2.2	Fatigue.....	12
2.3	Fracture Mechanics.....	13
2.4	Wavelet Analysis	15
2.5	Discussion	15
3	Preliminary Investigations	16
3.1	Instrumentation.....	17
3.1.1	Data Acquisition.....	17
3.1.2	Noise investigation.....	18
3.2	Transducer Calibration.....	19
3.2.1	Description of Transducer.....	20
3.2.2	Pencil Lead Breaks.....	20
3.2.3	Theoretical Comparison.....	22
3.3	Simulated AE Experiments.....	24
3.3.1	Half Space.....	24
3.3.2	Plate Edge	27
3.4	Discussion	32

4	Primary Experiments	33
4.1	Specimen Design and Preparation.....	34
4.2	Load Frames	37
4.2.1	Precracking Fatigue	37
4.2.2	Overload and Plastic Zone Tests	37
4.3	Instrumentation	43
4.3.1	Preamplifiers	43
4.3.2	Transducer Setup	43
4.3.3	Data Acquisition	44
4.4	Data Reduction and Analysis	45
4.4.1	Data Reduction Procedure	45
4.4.2	Determination of Seismic Surface Pulse Criteria	47
4.5	Test Procedure	54
4.6	Plastic Zone Tests	55
4.6.1	Load Regime	55
4.6.2	Results and Discussion	56
4.7	Overload Tests	59
4.7.1	Load Regime and Precracking	59
4.7.2	Results and Discussion	61
4.8	Summary of Results	66
5	Closure	67
5.1	Discussion	68
5.2	Accomplishments	72
5.3	Conclusions	73
5.4	Recommendations	73
	 References	 74
	 Appendix A Waveforms	 78
	 Appendix B LabView Program Documentation	 83
	 Appendix C Micrographs	 84

List of Figures

1.1	Mechanisms responsible for AE during material deformation	5
1.2	Transformation: Half-space to Full space with a crack	8
1.3	Nucleating micro-crack	9
3.1	Noise samples taken with and without preamplifier gain	19
3.2	Pencil lead break shoe on a 0.3 mm mechanical pencil on the left	21
3.3	Pencil lead extension fixture	21
3.4	Load profiles of ten pencil lead breaks	22
3.5	Theory vs. experiment of PLB on aluminum plate using NIST transducer	23
3.6	NIST transducer setup on large steel block	24
3.7	View of NIST transducer inside of Faraday shield box	25
3.8	Surface wave amplitude vs. distance from PLB on large steel block.....	26
3.9	Velocity calculation of PLB response on large steel block	27
3.10	Steel plate setup for testing PLB propagation on edge	28
3.11	Amplitude vs. distance from PLB on edge of steel plate	29
3.12	Velocity calculation of PLB response along plate edge	30
3.13	Amplitude of PLB spike versus filtering cutoff frequency	31
3.14	Thumbnail: Wavelet analysis of PLB edge wave	31
4.1	Modified ASTM E399 compact tensile specimen profile	34
4.2	Overall photo of Modified creep frame for overload tests	38
4.3	Weight pan end of the modified creep frame with pneumatic actuator extended	39
4.4	Manual control valve for the pneumatic actuator	39
4.5	Steel cable loop connection between weight pan and lever arm	40
4.6	View of one of the degree of freedom fulcrums with rubber pad installed	41
4.7	Load profiles vs. weights applied	42
4.8	Specimen installed in load clevises with transducer support arms attached	43
4.9	Specimen installation with Faraday shield boxes installed	44
4.10	Determination of AE signal history at the transducers vs. crack length	49
4.11	Calculated time delay between signals on channel 1 and channel 2	51
4.12	Thumbnail: Wavelet plot of filtered PLB on plate edge	52
4.13	Thumbnail: Wavelet plot of A2 ($R_c=60$) event from rapid brittle failure	53
4.14	Load profile for plastic zone tests	56
4.15	Surface deformation of the A36 plastic zone specimen	57
4.16	Stress intensity progression during load regime with preload and overloads 1-14	60
4.17	Thumbnails: Wavelet plots of 1018o10 AE event: channels 1 and 2	62
4.18	Thumbnails: Wavelet plots of A514 overload 1 event 038: channels 1 and 2	63
4.19	Thumbnails: Wavelet plots of A514 overload 4 event 022: channels 1 and 2	63
4.20	Thumbnails: Wavelet plots of A514 overload 9 rep 1 event 024: channels 1 and 2	63
4.21	Thumbnails: Wavelet plot of A2 ($R_c=50$) overload 1 AE event: channels 1 and 2	65
4.22	Thumbnails: Wavelet plot of A2 ($R_c=60$) overload 2 AE event: channels 1 and 2	66

List of Tables

4.1	Steel test specimen properties	35
5.1	Summary of AE tests	70
A.1	The four-panel plots	80
A.2	The low frequency component spectrum plots	81
A.3	The wavelet analyses	82
C.1	Micrographs	85

Preface

The introduction in chapter 1 describes the problem and illustrates the solution that was the impetus for the research. Chapter 2 outlines some of the general background of the fields of endeavor relevant to the research. Those with some knowledge of wave propagation in solids, fracture mechanics, fatigue, and wavelet analysis could probably skip that chapter. Preliminary experiments presented in chapter 3 set the stage for the main effort in chapter 4.

The reader should note the blue text or blue outlined thumbnail figures, which are links to items in other files. Some of the items are more easily presented in a different format than the main body of the document.

Usually for technical presentations, only the pertinent results are presented. The spirit, if not the letter, of that philosophy is followed in this document. However, this is a dissertation, an illustration of the research capabilities of the author. It is a compilation of all that went into this endeavor. Because of the particular type of research being pursued large amounts of information were developed from what would seem to be a small number of experiments. For completeness, a database of the results are in separate files accessible through links in the appendices. The database includes the listings for the computer programs written, plots of the waveforms collected, subsequent data reduction results, micrographs, and other "data" pictures. These files are rather large, so, this format allows the option to not download them.

Chapter 1

Introduction

In situations where catastrophic failure of critical members of larger structures is of concern, it is imperative to be able to evaluate the criticality of propagating cracks. In many real world situations, such as random overload and/or structure redundancy, crack propagation rate is unpredictable and crack length is not always a unique indicator of the state of the crack. Acoustic emission (AE) generated during deformation of most materials has long been promoted as a means of evaluating fatigue cracking. In reference to the state of a crack, "crack criticality" will be used in this discussion as the probability that the member containing a crack will fail catastrophically during the next load cycle in fatigue. The existence of specific modes of wave propagation in specific fatigue conditions may enable tracking crack criticality without knowing crack length.

This effort has been research into some of the fundamental aspects of AE from crack extension as the crack approaches final failure. Large steel structures like bridges are typically constructed from plate-like components, so the emphasis will be on cracks that have penetrated the thickness of a plate and are propagating in the plane of the plate.

1.1 The Problem of Crack Propagation

The research described here is an outgrowth of a previous investigation, by Duke, Sison, and the author [1996] to continuously gather AE waveforms from a crack on an existing heavily traveled bridge, in an effort to discriminate crack extension AE from other crack noises.

At first glance, the "ultimate" solution to the cracking problem would be to develop resistance to micro-cracking (crack initiation). However, the very things that lead to micro-cracking, such as dislocation motion or inclusion fracture, are also the processes that increase ductility of the material and hence toughness of the structure to withstand overloads. As reported by Lindley and McCartney [1981] many of the microstructural factors that increase resistance to crack initiation also contribute to increased fatigue crack growth rates. Therefore, resistance to crack initiation seems to be contraindicated in situations of "unknown" intermittent overloads that might be of significant magnitude to initiate cracking.

Since eliminating crack growth is possibly not feasible in many situations, another approach could be to predict the lifetime of a fatigue crack based on some knowledge of the loading history. The number of cycles spent in the final accelerating stage of fatigue is small in comparison to the other stages. Hence, much of the research of fatigue crack propagation rates has been concerned with the early and middle stages of crack initiation and propagation, a small portion of which has been reported in compendiums edited by Beevers [1980], Amzallag [1994], Ruschau and Donald [1995], and Marsh, Smith and Ritchie [1991]. In addition, the typical investigation reported in the literature has been concerned with life prediction under constant amplitude and constant frequency sinusoidal fatigue loading. An attempt to address more variation in loading, as reported by Khan, Rauf, and Younas [1997], shows that the fatigue lifetime of AISI 304 stainless steel subjected to simple sinusoidal "subthreshold" fatigue loading with periodic overloads, varies with the amplitude and periodicity of the overload.

1.2 Possible NDT to Measure Crack Extension

If we cannot predict lifetime unless we know the exact load history, how about using the crack length measurements to assess the crack criticality? Nondestructive techniques have been reported for measuring crack extension "in situ". Following are discussions of these techniques.

1.2.1 Acoustic Microscopy

A focused ultrasonic beam is acoustically coupled to the specimen and is scanned across the face of a specimen. The leaked/reflected energy from Rayleigh wave propagation is used to generate an image of the surface and subsurface. Jenkins and Briggs [1991] have presented a tutorial/overview about using acoustic microscopy for the detection and measurement of cracks. Karpur, et al [1995] has used acoustic microscopy to study the interfacial damage development of fatigued metal matrix composites. The technique is capable of submicron resolution, but the drawback is that the image is essentially due to the surface properties and cannot image the profile of the crack deep in the specimen. The high resolution necessitates isolation from the surroundings. Therefore, current commercial acoustic microscopes are large multi-component instruments for use only in a laboratory setting.

1.2.2 Ultrasonic Tip Diffraction

This technique also uses active ultrasonic interrogation for measuring the location and shape of the crack tip. Tip diffraction is different from acoustic microscopy in that the crack can be imbedded deep in a specimen. The technique has been reported to have sub millimeter accuracy by De Vadder, Park, and Francois [1995]. In their implementation, a focused transducer is acoustically coupled to the specimen through a water bath that surrounds the specimen. The transducer scans the specimen in a plane approximately parallel to the plane of the crack surfaces. The transducer fixture has three axes of motion control that allows the transducer to be oriented relative to the specimen such that no specular reflections from the crack can be received back at the transducer. The only way energy can be received by the transducer is from energy diffracted by some discontinuity in the path of the sound beam, in this case the crack tip. Since the anomalous region, involved in the diffraction, is smaller than the rest of the crack surface involved in the specular reflection, then the precision in finding the location of the tip is much improved over other ultrasonic techniques.

1.2.3 Potential Drop

This method for measuring fatigue crack propagation depends upon an applied electric field and the resultant current flowing from one side of the crack to the other. This current flow is a function of the specimen geometry, crack length and many other factors. As stated by Donald and Ruschau [1991] "... reliable implementation of the technique is not (simple)", "... special

care must be taken to minimize electrical noise, thermally induced EMF...", and "Measurements may also be susceptible to ... shorting across the fatigue crack surfaces, current and potential lead attachment, fixturing, dynamic loading, temperature and environment".

1.2.4 Compliance

These methods, reported by Fleck [1991], use direct measurements of displacement on various regions of the specimen under load. Displacement gauges are typically mounted near the crack tip, across the crack mouth or on the back face of the specimen opposite the mouth. The near tip mounted gauges measure compliance at the tip and not crack length. They have limited usefulness for long term monitoring, because, as the tip moves relative to the gauge, the calibration changes. Back face strain gauges are only useful for simple geometry specimens in bending, such as compact tensile specimens or four point bend. These methods are of obviously limited use where cracks exist in members with a variety of shapes and sizes. Crack Mouth Opening Displacement (CMOD) gauges require a priori knowledge of the existing crack length to be properly calibrated for tracking crack extension. The primary concern with compliance methods is that accurately tracking crack lengths require calibration curves that are not independent of specimen geometry and state of stress.

1.2.5 Acoustic Emission

Crack propagation investigations using acoustic emission have tended to focus on two areas. One is about the parametric description of the AE signal shape. A whole lexicon of AE parameters has developed to describe the activity coming from a crack [Pollack 1996]. The other is about triangulation of the crack location using multiple sensors arranged at known locations.

Monitoring AE activity during fatigue is troublesome, because there are many sources for that activity that are not due to crack extension. These "secondary sources" have been discussed by Scruby and Buttle [1991] and include crack rubbing/fretting, crushing of particulate/corrosion products, and crack closure/unsticking. As to primary sources, crack extension in ductile steels can initiate by precursor micro-cracking of hard inclusions. These events can be energetic enough to generate detectable AE, but they occur ahead of the crack tip. According to Ohira and Pao [1989], they can occur ahead of the plastic zone. Actual extension occurs when the intervening ligaments tear (void coalescence). These are ductile events and not very energetic. Data reported in a survey by Dunegan [1987] and replotted in Figure 1.1, show that the ductile mechanisms of slip dislocation motion, twinning, and martensitic phase transformations are 10 to 60 dB (10 dB = 3.2x, 60 db = 1000x) smaller than the brittle fracture mechanisms of hard inclusion fracture, oxide fracture, intergranular cracking, and cleavage cracking. Hence, not all detectable AE can be immediately attributed to the final generation of new crack surface. However, it should be noted that those discussions were concerned only with the bulk wave mode emissions from imbedded sources.

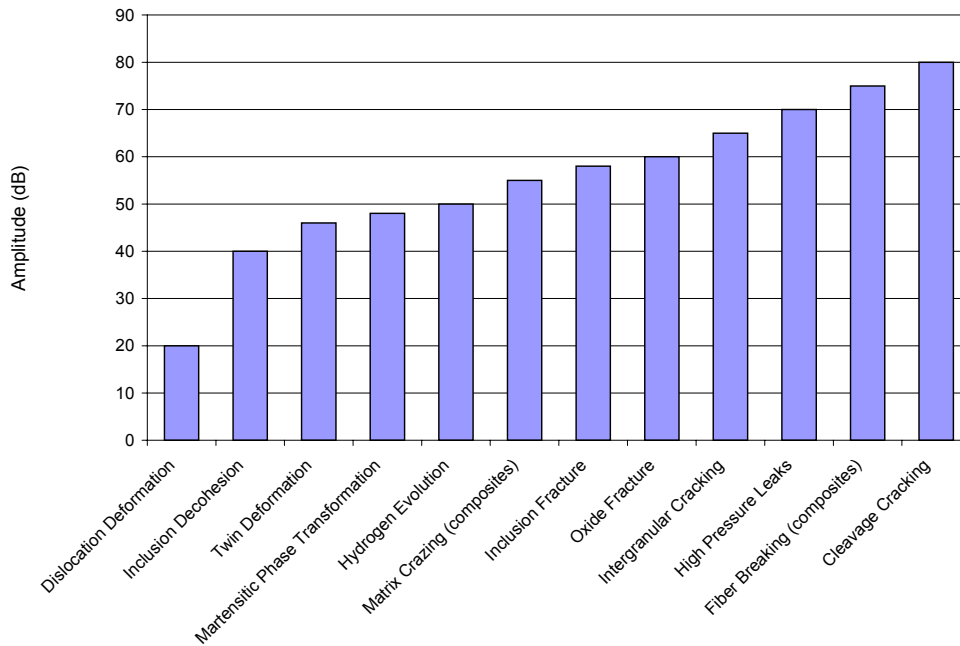


FIG. 1.1. Mechanisms responsible for AE during material deformation and their typical AE signal amplitudes.

The traditional implementation of source location requires knowledge of the velocity of the wave propagation of the signals received by the sensors in the grid to accurately triangulate the source of the sound. The relative amplitudes of the different modes of wave propagation in a material can vary significantly, depending on the orientation and type of disturbance generating the waves. Therefore, it is difficult to decide what type of wave has arrived, hence invalidating the triangulation calculations. A technique using moment tensor analysis of the AE has been developed and has been surveyed by Enoki and Kishi [1991]. A moment tensor can be generated from two vectors, which define the crack kinematics, and the elastic constants. The crack kinematic vectors are the direction of the crack normal and the direction of the crack displacement. The waveform at any point in the body can then be described by a set of equations with six unknowns. To solve these equations for the location of a sound source requires;

- 1) Data from at least six sensors,
- 2) Knowledge of the exact location of these sensors,
- 3) Small source size compared to the distance to the closest sensor,
- 4) The Green's function for the specimen.

The Green's function, which characterizes the impulse response of the specimen, is a function of the exact size and shape of the specimen and is difficult to develop analytically for anything other than a simple geometry. In addition, as mentioned by Ohira and Pao [1989] the length of the micro-crack cannot be directly measured. It has to be deduced from the amplitude of the signal, which is related to the volume of the micro-crack. That consideration along with the fact

that using this technique in fatigue studies would also locate all the secondary sources of AE, leads one to conclude that an accurate location of the crack tip would not be possible.

1.2.6 Summary

Each of the different crack length measurement techniques discussed previously have disadvantages for use in the field, which possibly could be overcome with further engineering improvements. For use in the laboratory, as means to nondestructively indicate crack length, they have potential, but are not developed enough to produce the "smoking gun", i.e., a specific cracked particle or crack extension for a particular AE event. However, the primary drawback to crack length measurements is that once the crack length is known, the measurement has to be interpreted in some manner to evaluate the criticality of the crack. There are many real situations where the length of the crack is not a unique indication of its criticality. For example, in redundant structures, increased deformation during load excursions of the cracked member can be sufficient to transfer enough load to the other members and the crack propagation rate slows significantly. For life prediction, this might not be a problem if the crack length measurements are simple, continuous and accurate. Hence, one would know that the crack has arrested. It is felt that none of the direct measurement techniques just discussed has that capability yet. Of the indirect measurements, traditional AE techniques still doesn't measure up, because as fatigue loading continues, the crack still opens and closes and possibly generates secondary AE of the type discussed in Section 1.3.5, even though the propagation may be slowed substantially.

In summary, cracking in randomly loaded structures is almost inevitable. The fundamental approach of relating the crack length measurement to the crack criticality is fraught with problems of uniqueness and the need to measure accurately and continuously. Predictive approaches could eliminate some of the length measurement problems, because that phase could be done in a laboratory setting for "calibration/corroboration" purposes. However, any real structure typically has a loading history somewhere between the extremes of simple continuous sinusoidal loading and completely random "white noise" loading. Historical AE investigation has problems with distinguishing between and deciding the uniqueness (as related to the state of the crack) of the AE from plastic zone formation, new surface generation, and secondary sources. So, it was felt that because the state of stress of the crack changes with criticality, regardless of crack length or load history that investigation of the change in energy emitted during crack extension has the potential to evaluate criticality.

1.3 Measuring Criticality Directly

Is it possible that measuring energies released from the crack tip during propagation can monitor crack criticality?

Studies in brittle materials, where fracture did not occur in fatigue, by Thaulow and Burget [1990], Theocaris [1989], and Kamath and Kim [1986], have reported the generation of Rayleigh waves, which propagate away from the tip of an unstable propagating crack, back along the crack faces toward the mouth. These waves have sufficient energy to momentarily arrest a fast moving brittle elastic fracture crack by reflecting off the crack mouth, traveling back toward the tip and reducing the stress concentration at the tip due to wave interference [Thaulow and Burget 1990]. This has been shown for PMMA (polymethylmethacrylate, i.e., Plexiglas) under monotonic loading conditions (by the above mentioned authors), and thin plates of high strength steel [Rossmanith and Fourney 1982].

Consider a highly idealized thought experiment. It has been calculated by Miller and Pursey [1955] that for a disturbance due to a circular disk vibrating normal to the surface of an idealized half space (Poisson's ratio = 0.25), less than 7% of the of energy carried away by wave propagation is in the bulk compressional wave. However, over 67% is partitioned into surface waves and the remainder into bulk shear waves. Imagine stretching the circular disk into a more linear source, and folding the surface of the half space along the center line of that source, to generate a full space with a "crack", as shown in Figure 1.2. This leaves the source in the fold or "crack tip". The original vibration normal to the surface of the half-space has become an expansion/contraction or dipole motion at the crack tip in the full space. It would seem that the motion of this source could be a model for the disturbance generated by the release of energy during an idealized "instantaneous" crack extension event.

Admittedly, assuming that the crack extension occurs rapidly with a simple macroscopically linear crack front, completely ignores the fact, as mentioned previously, that crack extension in ductile steels can occur due to ductile tearing of ligaments between micro-cracks ahead of the crack tip. In other words, the crack extension does not occur as a single macroscopic disturbance across the entire crack front. However, (for a final fracture in fatigue that is a fast propagating failure) it is felt that as a crack approaches the final failure conditions, it is exhibiting more and more characteristics of fast failure. Steels exhibit a transition from ductile to brittle behavior, with increasing strain rate [Dowling 1993]. For a given load cycle, as the crack gets longer and approaches failure, the net section stress increase after each increment of crack extension becomes more and more significant. Does the local strain rate (on the scale of the microstructure) near the tip increase enough that the crack switches from ductile to quasi-brittle behavior prior to final failure? If so, the generation of surface waves that occur during catastrophic brittle failure, could appear, albeit weaker, several cycles before. Calculations by Achenbach and Harris [1979] show that AE is more intense the higher the speed of the crack tip, and when stress level near the tip is higher. As the crack approaches criticality, AE changes. Are there other changes besides intensity and can we detect them?

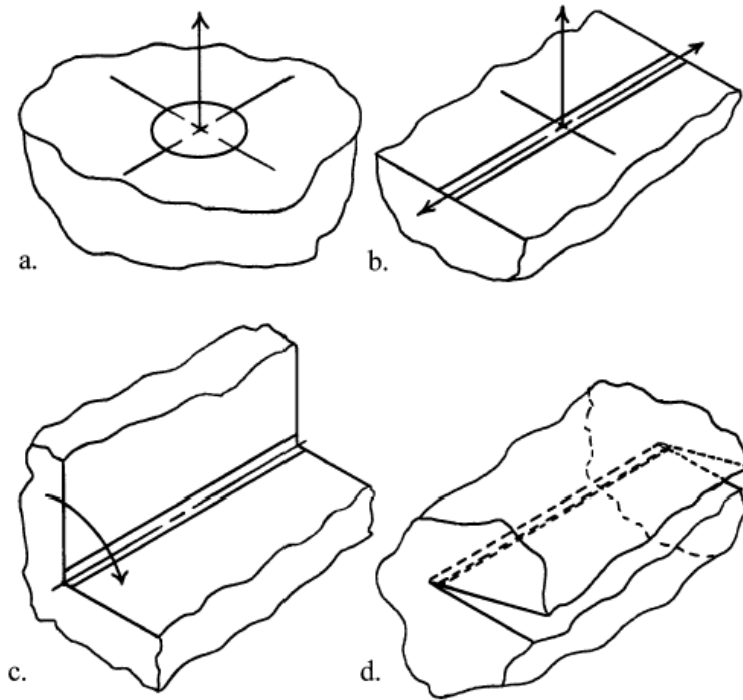


FIG. 1.2. Transformation: a) vibrating disk on half-space to b) vibrating "linear" source to c) folded space to d) full space with a crack.

Furthermore, if the final failure is ductile, it may still be possible that Rayleigh waves are generated prior to that event. Achenbach, Hirashima, and Ono [1983] has formulated that acoustic emission signals, generated when a micro-crack nucleates in the vicinity of an existing macro-crack, as shown in Figure 1.3, tend to be larger than those from the micro-crack by itself. This effect is due to an elasto-dynamic interaction between the two cracks, where the opening of the micro-crack generates additional momentary opening of the macro-crack, which in turn generates additional opening of the micro-crack. Generation of surface waves on the faces of the macro-crack was not considered. The formulation assumes the AE is a function of the crack-opening volume with time and only considers the waveform generated at 90 and 45 degrees to the crack face. In the simulation, this effect is enhanced as the length of the macro-crack is increased, becoming much larger than the micro-crack length, and as the micro-crack is located closer to the macro-crack. The calculations were of macro-crack over micro-crack length ratios (l/l_m) up to 1000, and macro-crack-length over distance-to-micro-crack ratios (l/e) up to 1000. It is stated, that for the length and distance ratios of 1000, the macro-crack generates an additional signal that is over an order of magnitude greater than the micro-crack signal and the coalescence of the two produces a signal over two orders greater. Hence, it may be possible, except in

fracture that is completely ductile, that void coalescence, if it is rapid enough, could actually produce detectable surface wave propagation on the macro-crack faces.

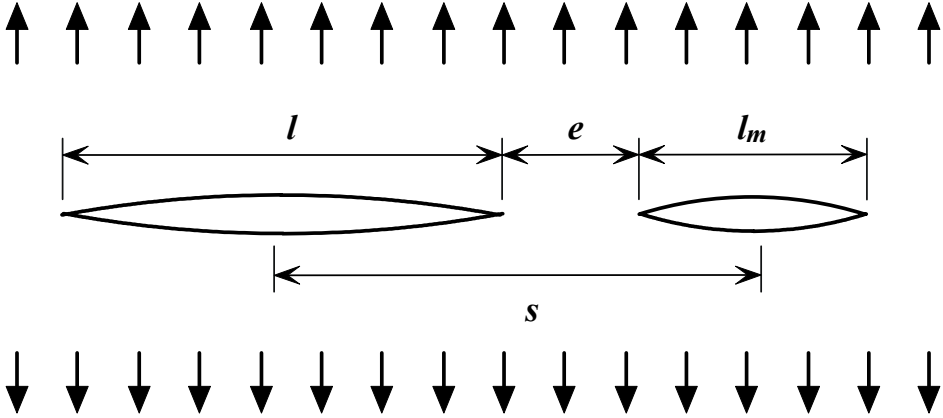


FIG. 1.3. Nucleating micro-crack, l_m , in the vicinity of an existing macro-crack, l .

Chapter 2

Theoretical Considerations

2.1 Wave Propagation

2.1.1 Rayleigh Waves and the Seismic Surface Pulse

Consider a linear elastic homogeneous isotropic material half space. Other than the waves with longitudinal and transverse particle displacement (relative to the propagation direction) in the bulk, this half space can support waves on its surface. One particular type, called the Rayleigh surface wave [Victorov 1967] is a solution satisfying the boundary conditions of no surface traction, the wave equation, the constitutive equations, and the assumed form of a propagating wave which decays exponentially away from the boundary while it propagates along the boundary. It has components of displacement both normal and parallel to the surface, such that particles at the surface follow an elliptical retrograde motion with the ellipse's major axis normal to the surface. The horizontal motion decays with depth and is zero at a depth of approximately 0.18 times the Rayleigh wavelength. Below this depth the horizontal motion reverses, hence the elliptical particle motion is in the opposite direction. The velocity of the wave is only a function of Poisson's ratio and not frequency. Therefore, it is non-dispersive. Over the range of possible values of Poisson's ratio, 0.0 - 0.5, the velocity varies from 0.87 - 0.96 times the velocity of the bulk transverse (shear) wave. The depth of penetration varies with the frequency of the waves; the motion decaying to almost nil at a depth of twice the Rayleigh wavelength. The most interesting property, relevant to the detectability of surface waves, is the 2-D nature of the energy propagated by the wave. From energy flux calculations, one finds that the energy flows out from and back to the surface as the wave propagates. The net energy leaking into the bulk material is zero and, so, the amplitude reduction due to radiation spreading is of the order of $1/R$ (R = distance from source) vs. $1/R^2$ for bulk wave propagation modes. Anisotropy, surface roughness, viscoelasticity all affect surface wave propagation by introducing behavior such as more complex particle motion, frequency dependence (dispersion) and energy leakage into the bulk of the specimen.

Now consider the case of a seismic surface pulse (SSP), which is the response to a step unload at a point on a half space, introduced theoretically by Pekeris [1955]. As the energy radiates from the source location, the response on the surface at any point away from the source sees three modes of wave propagation pass by. The first is the head of longitudinal bulk mode

radiating from the source, then the head of the shear bulk mode that is traveling at approximately half the speed of the longitudinal mode. Quickly following the shear mode is the Rayleigh surface wave component. Experimental results by Proctor [1982] show at least an order of magnitude larger surface displacement for the surface wave component over the longitudinal component for the distances they were investigating. This is to be expected because first, the longitudinal mode is carrying much smaller amount of energy (as noted previously) and second, the propagation direction of the longitudinal component near the surface is essentially parallel to the surface, hence, the particle displacement is also parallel to the surface. In addition, the beam spreading, noted above, reduces the displacement of the bulk waves much faster than the Rayleigh component.

The previous discussion has shown that detecting the arrival of a surface wave component versus the longitudinal wave (from the same source), on the same surface, is much easier due to the larger normal displacement of the surface wave. Now, consider the difference between detecting the surface wave versus detecting the longitudinal pulse elsewhere on the specimen. Since Poisson's ratio, which is the ratio of transverse to longitudinal strain, is approximately 0.3 for metal alloys (0.29 for steel, and 0.34 for aluminum), the longitudinal strain for the longitudinal wave at any point in the body will only be approximately 3 times the transverse strain at the surface (the strain detected by the transducer in the same-surface experiments). This still does not compensate for the much larger displacements of the surface wave.

2.1.2 Edge Waves

Because of the geometry of a crack propagating in a plate, in other words, two boundaries perpendicular to the crack surfaces, it is plausible that the wave propagation on the crack surface is not a surface wave, but a type of edge wave as introduced by McCoy and Mindlin [1963].

2.2 Fatigue

For all cracks that propagate intermittently in materials that exhibit some ductility, there are different regimes of propagation. Different types of processes occur in those regimes, as reported by Lindley and McCartney [1981]. Three regimes (or stages) become evident, when one looks at crack growth rate (per cycle) as a function of the range of stress intensity (a measure of the severity of the crack) at the crack tip.

At low stress intensity range, in stage I, crack propagation is highly influenced by mean stress, microstructure and environment. This stage, for some materials, supposedly has a lower bound called the fatigue crack growth threshold, which is the minimum stress intensity range below which growth does not occur. In this stage, one is primarily concerned with crack initiation.

In stage II of constant growth rate, the rate is not as influenced by the factors that influence stage I behavior. Classic striation formation of the fracture surface, where each striation relates to one fatigue cycle, occurs in this stage. However as noted in the literature [Boyer 1975], even though each striation is due to one fatigue cycle not every fatigue cycle creates a striation.

At high stress intensity ranges in stage III, behavior is again highly influenced by microstructure and mean stress. Static mode fracture mechanisms, in other words, the mechanisms that occur during monotonic tension as a material is pulled to failure, begin to occur in this regime. The growth rate increases asymptotically in this regime to an upper bound that approximately corresponds to the static fracture toughness. In other words, if the maximum stress intensity of the fatigue cycle approaches the fracture toughness of the material the growth rate approaches unstable fracture.

Stress intensity increases rapidly when the crack length becomes a significant percentage of the specimen size. Therefore, the number of cycles spent in stage III before final failure is very small compared to the initiation and constant growth regions.

2.3 Fracture Mechanics

Fracture of any material at temperatures well below a transition zone, typically called the ductile to brittle transition for polycrystalline materials and the glass transition for polymeric materials, or in an "embrittled" condition due to other considerations such as hydrogen "embrittlement" or stress corrosion exhibits very little permanent or plastic deformation on a macroscale. In these conditions, microstructure is less of a factor and the "brittle" failure occurs rapidly and catastrophically. For "brittle" steels, this occurs when a stress intensity of approximately $40 \text{ ksi}\sqrt{\text{in}}$ is reached at any point [Dowling 2003]. However, brittle failure is not classified by the fracture toughness value alone. Ceramics at room temperature typically fail at stress intensities below $5 \text{ ksi}\sqrt{\text{in}}$. Aluminum alloys at room temperature rarely have fracture toughness above $40 \text{ ksi}\sqrt{\text{in}}$.

However, any material that can sustain even a moderate amount of fatigue, under cyclic loading conditions, has plastic behavior occurring at the crack tip. In other words, that section of material goes through the elastic region of stress-strain behavior, past the yield point into plastic flow. This reduces the stresses, that is, relaxes and blunts the tip allowing it to withstand the current load cycle without continued rapid fracture.

Time is also a factor to determine whether fatigue or catastrophic failure occurs. If there is insufficient time during a load cycle for the plastic flow at the tip to relax the high tip stresses, the failure transitions from ductile to brittle [Boyer 1975]. In addition, typically as strain rate increases the yield stress increases and plasticity decreases.

The size of the plastic zone around the tip where plastic flow has reduced the stresses is a function of the yield stress, the stress intensity, and the triaxiality of tip stresses. In thin materials under planar loading, there is not enough material through the thickness to constrain the Poisson effect strain; hence, the stress perpendicular to the plane of the plate is essentially zero. This condition is called plane stress. As the thickness of a material increases the constraint increases and a portion of the thickness in the interior has zero strain, hence non-zero stress, in the thickness direction. This condition is called plane strain. The increased triaxiality of the stresses toward a state of hydrostatic tension constrains the plastic flow, therefore increasing the possibility of brittle failure.

The plastic zone size for these two conditions can be calculated [Dowling 1993]; with the primary distinction being the plane stress plastic zone size is three times the plane strain zone size. If one thinks about the boundary condition of zero normal stress at the surface of a thick plate, one realizes that the plastic zone diameter around the crack tip, at the surface, is indicative of a state of plane stress. Hence, it is largest at the surface. The zone diameter decreases rapidly and approaches that of a state of plane strain, as one goes into the material. Hence, the extent of changes of the surface of properties that are a function of the plastic flow, say, surface displacements or surface texture, can be used to estimate the plane stress plastic zone size regardless of the thickness of the material.

For real structures of limited size, failure can be classified into several regimes [Dowling 1977] depending on your definition of failure: plastic limit load, nominal yield, and fracture toughness ("brittle"). Nominal yield assumes that we want no yielding at all in the cross section.

In other words, the point of highest stress in the cross section is taken just to yield. If yielding is allowed to occur, plastic limit load is the load when all the cross section reaches yield. For failure of a brittle nature the failure surface exhibits no shear deformation. The load at failure is governed by fracture toughness. The surface has no dimpled facets or slanted sections (to the axis of maximum normal stress). It exhibits transgranular or intergranular cleavage and the plane of the surface is normal to the axis of maximum normal stress. [Boyer 1975]

2.4 Wavelet Analysis

Much development and discussion of wavelets has occurred in the last 20 years since the term was coined in the 1980's. Since then, mathematical formalism has expanded the umbrella of wavelets over other already existing multiresolution analyses. Two excellent books by Debnath [2002] and Nievergelt [1999] present historical development, some theoretical support and applications of wavelets.

As a Fourier integral transform can transform data localized in time to data localized in frequency, a Wavelet transform can be used to describe the energy density of a signal localized in both time and frequency.

Since the interest in wavelets for this research is of a practical nature, a theoretical development is not pursued. Instead, a presentation of the effects of a wavelet transform on some well characterized signals is presented; [40 kHz sine wave](#), [noisy sine wave](#), [triangle wave](#), and what will be called a [warble](#) (where pitch oscillates, in this case linearly increasing with time then linearly decreasing) all sampled at 100 MHz. This particular implementation of a wavelet transform was supplied by Vallen-Systeme GmbH, and uses the Gabor transform, which is essentially a short time Fourier transform. Conceptually, a small window of time is stepped along the signal of interest, an FFT taken at each step, and the results plotted on a 2-D plot of frequency vs. time. The wavelet settings are 10 kHz frequency resolution and a length of 200 samples (the entire length of the signals is 8000 samples).

Note the inability to accurately characterize at zero crossings in the time domain. In addition, an echo effect exists in the frequency direction. However, to be fair, these are extreme examples of small wavelet size versus the "cycle" size of the signals. Note as one approaches the wavelength in the sine wave (2500 samples) in wavelet plots with wavelet lengths of [800](#) and [1600](#) samples, that the frequency accuracy increases and many of the artifacts (echoes and no zero crossing data) disappear.

2.5 Discussion

The highlight of this chapter is that there is research that indicates the Rayleigh component of the SSP, measured normal to the surface, starts out at least 10 times the amplitude of the longitudinal wave component. The displacement of the longitudinal wave component in the direction of propagation (perpendicular to the surface) is approximately 3.4 times (for steel) the transverse displacement (normal to the surface). Therefore, the initial amplitude of the Rayleigh component is at least 3 times the amplitude of the longitudinal component measured in the direction of propagation.

Chapter 3

Preliminary Investigations

The desire to detect AE regardless of amplitude and somewhat regardless of time of occurrence suggested that some experiments be performed on candidate AE equipment to determine their capabilities. Traditionally, data acquisition is activated (triggered) when the amplitude of the incoming signal, compared to a constant value (threshold), is above that threshold. If the amplitude of an AE event is approximately the same as the background noise in the signal then threshold triggering is out of the question.

In addition, the effects of boundaries on wave propagation needed to be studied because the specimens used are small enough that theoretical assumptions of half spaces are not valid.

It should be noted that some preliminary AE tests were conducted on steel specimens of the geometry used in the primary experiments. They were of the following types of steel: 1018, A2 ($R_c=50$), A2 ($R_c=60$), and HPS70. These tests were invaluable in the development of the testing paradigm presented in chapter 4 by pointing out the need to change specific aspects of testing, such as better specimen preparation (metallographic polish) and the need for different data acquisition equipment. However those results will not be presented here.

3.1 Instrumentation

3.1.1 Data Acquisition

During the course of these preliminary investigations, which helped develop this new testing paradigm, four data acquisition systems were used and evaluated before the final solution was used for the primary testing presented in a later chapter. One system was from Physical Acoustics Corp. (PAC) and three from Gage Applied Science, Inc.

Uninterrupted acquisition, for most digital data acquisition systems, is limited by the amount of high-speed memory that allows the data acquisition to continue sampling until the memory is filled up. To understand the meaning of "uninterrupted acquisition" or "continuous sampling" one must realize that sampling is inherently a discretized process. Therefore continuous or uninterrupted does not imply that data is being recorded in the analog meaning of continuous (as on a tape recorder). It does imply that the data acquired has been sampled at a constant sampling rate. Every data point is sampled at the same time increment from the previous and subsequent ones. One has to be careful about this concept because some digital systems may have settings that allow long periods of data acquisition, but, it is possible, that they are not doing it continuously or uninterrupted. Tricks such as circular buffers and quiescent time offloading notwithstanding, high speed memory capable of keeping up with the throughput of the analog to digital convertors eventually fills up and has to be offloaded to permanent storage. For data acquisition cards that are designed to be installed in a PC this high speed memory typically is not the computer RAM, but dedicated memory installed on the board itself. Once full, this memory then has to be offloaded to RAM or the hard drive of the computer. Typically, this is a "dead time" when the data acquisition is not waiting for the next trigger and hence cannot acquire data.

Several tests were performed with the PAC system to determine its dead time. The system can be set up with different testing parameters that allow one to vary the size of the data acquisition sample, the delay time between triggers, the sample rate, and the ability to trigger internally (without needing to monitor a signal for threshold crossing). The delay was set to the minimum and the internal trigger mode activated. After calculating the dead time using the time marks for each record (recorded to 0.1 μ sec), the record width, and the sample rate, it was a bit distressing to note the dead time could vary from 62% to 96%, as record length was varied. This system automatically offloads its data to files on the hard drive so it is plausible that a faster computer could reduce these numbers, but other factors, such as onboard filtering, also reduced its desirability for the current research effort.

The Gage data acquisition boards also have some of these limitations, if one uses them in the same manner. However, they are easily configured to trigger from an external trigger signal, such as a load cell signal. Once triggered, the board acquires data to the onboard memory without interruption. These boards are designed to have an enormous amount of memory, and, at this point in time, it is impossible to have hard drive speeds (if using the PAC system), that rival the speed of the Gage onboard memory. The three boards we have acquired over the course of this research are two 100 MHz boards of 12 bit and 14 bit sample amplitude resolution and one

10 MHz 16 bit board. They do not have onboard filtering that could distort the data. Another very important design feature is that each channel of data acquisition is independent of the other. This is accomplished by having duplicate electronics for each; there is no multiplexing or sharing of resources. Both channels can be triggered off the same input signal. Hence, any differences in arrival time of events of interest between the channels is a function of the original signals and not the electronics.

3.1.2 Noise Investigation

An investigation into the electronics background noise was conducted with the 14100 board (Gage 14 bit, 100 MHz). Shown in Fig. 3.1 are three examples of many samples of the inherent system noise that were taken under various conditions and configurations. The "No Preamp" trace was acquired without any equipment or transducers attached to the data acquisition ports. The two other traces are for an attached preamplifier, which was eventually chosen for the remainder of the tests. No transducer was attached and the gain settings were 20 dB (10X) and 40 dB (100X).

The amplitude of the data acquisition noise ("no preamp"), which should remain constant regardless of input signal level, seems to be, at most 0.5 mV, while the amplitude of the 40 dB trace is at most 5 mV. Note that the noise amplitude has only increased by about 10X while the available gain to an applied signal is 100X. Assuming the minimum detectable signal level in acquired data is on the order of the noise, then, even though the preamplifier has increased the noise level, it seems the minimum detectable signal (from the transducer) has improved from 0.5 mV to 0.05 mV (5/100 mV). Before the general criticism is leveled that "signal to noise ratio" is not improved by amplification, one should be careful to note where in the signal path the noise is injected. In this case, there is a constant level of noise from the A/D board. This noise (possibly from the computer it resides in) is added to the signal after preamplification, hence not affected by that preamplification. So, any amplification that brings the minimum detectable signal level (at the transducer) above that constant noise level improves the detectability.

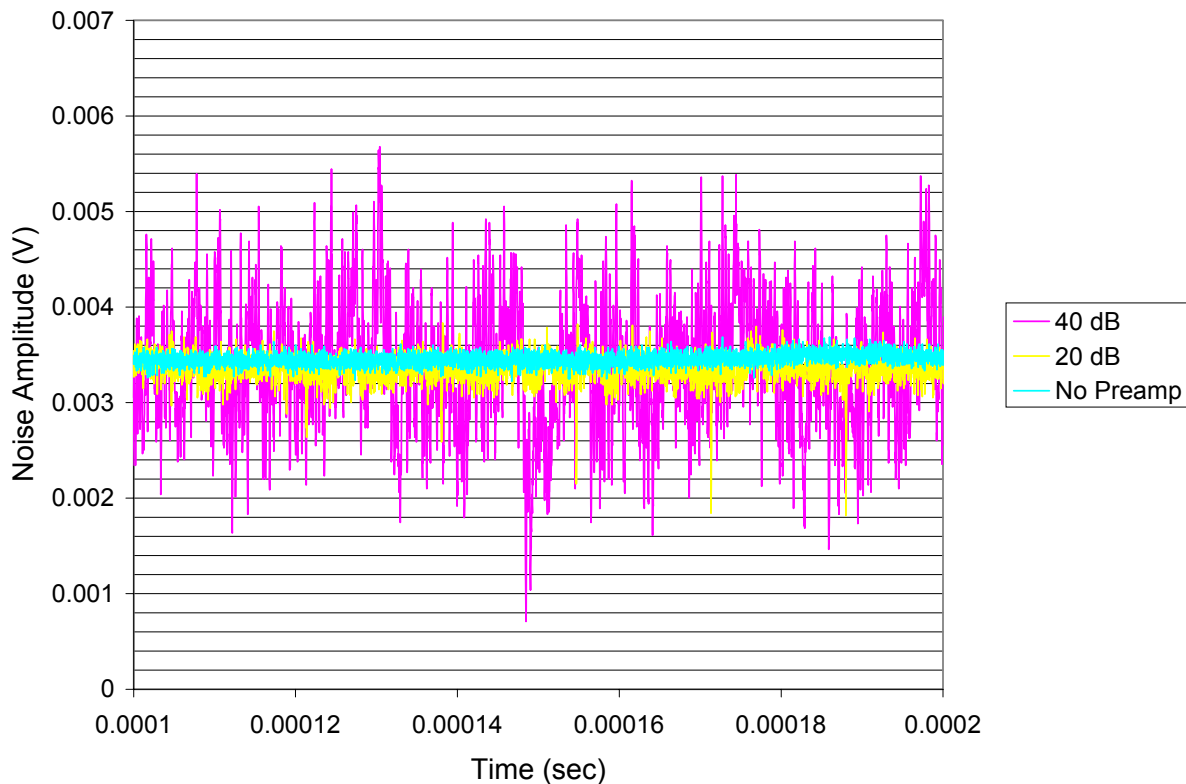


FIG. 3.1. Noise samples taken with and without preamplifier gain.

Because of this improvement, it was decided to use this preamplification with a gain setting of 40 dB. The PAC preamplifiers have their filter sections removed as per PAC instructions and replaced with a capacitor. In this wide band condition, they exhibit a 6 db drop-off bandwidth of almost 6 MHz starting from about 2.5 kHz. Since, they are not self powered, but powered through the connection with the PAC A/D board, custom circuitry was built to replace the power generation and DC blocking features, as per PAC instructions, to provide only a data signal to the Gage data acquisition system.

3.2 Transducer Calibration

3.2.1 Description of Transducer

The transducers used for this research are specialty items following a NIST design, so some description is warranted. The transducer is a point contact transducer from NIST [Proctor 1982]. It is constructed of a small, truncated cone of piezoelectric material, as the active element, attached to a large brass backing. The transducer fixture is designed such that there are three points of support. The primary point is the sensing cone itself. Two nylon machine screws (the heads are visible at the left end of the brass block, see figure 3.7) that go through the block and have machined tips, comprise the other two points of contact. The transducer is supplied with an impedance matching buffer amplifier, which has a gain of approximately 1, that allows the output to be connected to typical data acquisition systems with 50 ohm input impedance. The tip of the active cone is plated with nickel and acts as the one electrode for the sensing element. It is located on the right end of the brass block approximately just below the small hole visible in the aforementioned picture. The large brass backing acts as the other electrode. It also acts as an inertial mass damper to reduce vibrations of the tip to its lowest frequency. The frequency response is from approximately 5 kHz to 1.5 MHz. It has been designed to be comparable to the NIST standard capacitive transducer that is used to calibrate all other transducers. Because the sensor itself is not shielded, the aluminum box as seen in figure 3.6, acts to isolate the sensor from ambient RF noise while also providing the ground path for the circuitry. Specimens must be conductive to provide circuit completion.

3.2.2 Pencil Lead Breaks

Pencil lead breaks (PLBs) are one of the suggested "standard" methods for testing AE sensor response in ASTM E976 "Standard Guide for Determining the Reproducibility of Acoustic Emission Sensor Response", and have been the subject of a significant amount of research. A small tip of a specific shape to be installed on the lead support tube of a mechanical pencil is described in that document. It allows one to break the lead consistently on the surface of a specimen producing a step unload at a "point". One of these tips was made, as shown in the Figure 3.2 installed on the end of a 0.3 mm mechanical pencil on the left compared to the unmodified pencil on the right, and used for all the PLBs in this research. The edge of the tip (the diameter of the cylindrical section) acts as a fulcrum while the back end of the pencil is pivoted up, breaking a section of extended lead in bending. The lead extension is specified to be 3 mm from the end of the support tube (which extends to the tip of the smaller conical section) and was set using a 3 mm deep flat bottom hole on the edge of a piece of brass shown in Figure 3.3.



FIG. 3.2. Pencil lead break shoe on a 0.3 mm mechanical pencil on the left.



FIG. 3.3. Pencil lead extension fixture.

To investigate consistency, a series of ten PLBs were conducted on the face of a small range load cell (10 N). The pencil rested on a stable support adjacent to the load cell with the lead tip contacting the load cell face and the lead broken in the same manner as regular PLBs. The load trace of each series is plotted in Fig. 3.4, on top of each other, with a 2 second offset between each one. Since the lead is pushed onto the load cell, the breaking points are the points of maximum compression that fall in a range of about 0.1 N around -0.75 N. The sections of high frequency vibration are the ring down responses of the load cell post-break. There was a concern that the slow sample rate of the data acquisition did not accurately capture the peak load at break.

By stretching the time scale to look very closely at the peak loads (valleys) it was decided, by extrapolation of the pre- and post-break sections of the trace, that a possible error due to not capturing the peak accurately is on the order of 0.01 N.

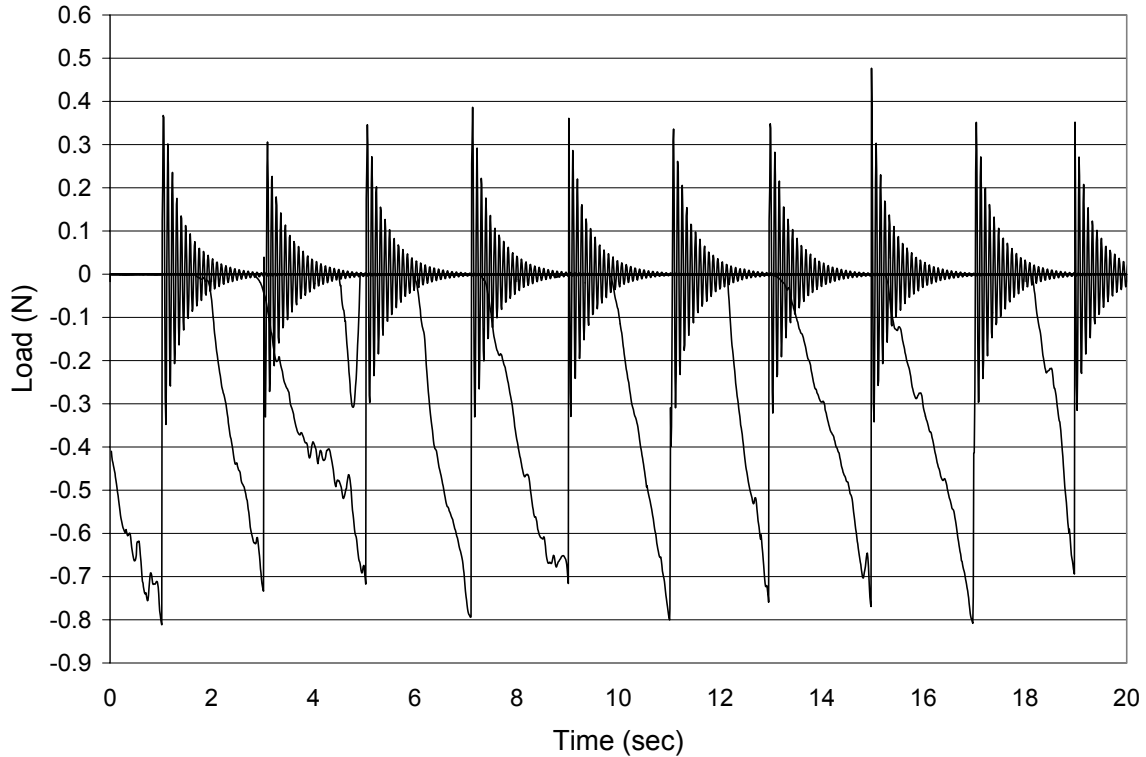


FIG. 3.4. Load profiles of ten pencil lead breaks (PLBs)

3.2.3 Theoretical Comparison

The fidelity of the transducer is indicated in Fig. 3.5 that shows the amplitude vs. time response of pencil lead breaks (no amplification) on an square aluminum plate compared to a theoretical response [Prosser 1999]. The experimental sensor to receiver distance was set to be the same as in the theoretical calculations. The earliest possible effect of reflections from the plate edge of the experimental data (calculated using longitudinal mode velocity) would occur at about $34 \mu\text{sec}$ after the break, i.e. at about $49 \mu\text{sec}$ "on" the plot. The theoretical Prosser plate is larger so reflections from the edges would occur even later. In other words, the boundaries of the plates are not a factor in this comparison. The theoretical PLB was 0.75 N, approximately the same as the actual PLB. The amplitude scales of the two traces were adjusted and time scale of each was shifted to get the first large peak (the one shown at $25 \mu\text{sec}$) to closely match. Note that

the frequency of the first four small excursions is approximately 500 kHz and is greater than the frequency of the subsequent large excursions, which seems to decrease as the amplitude increases.

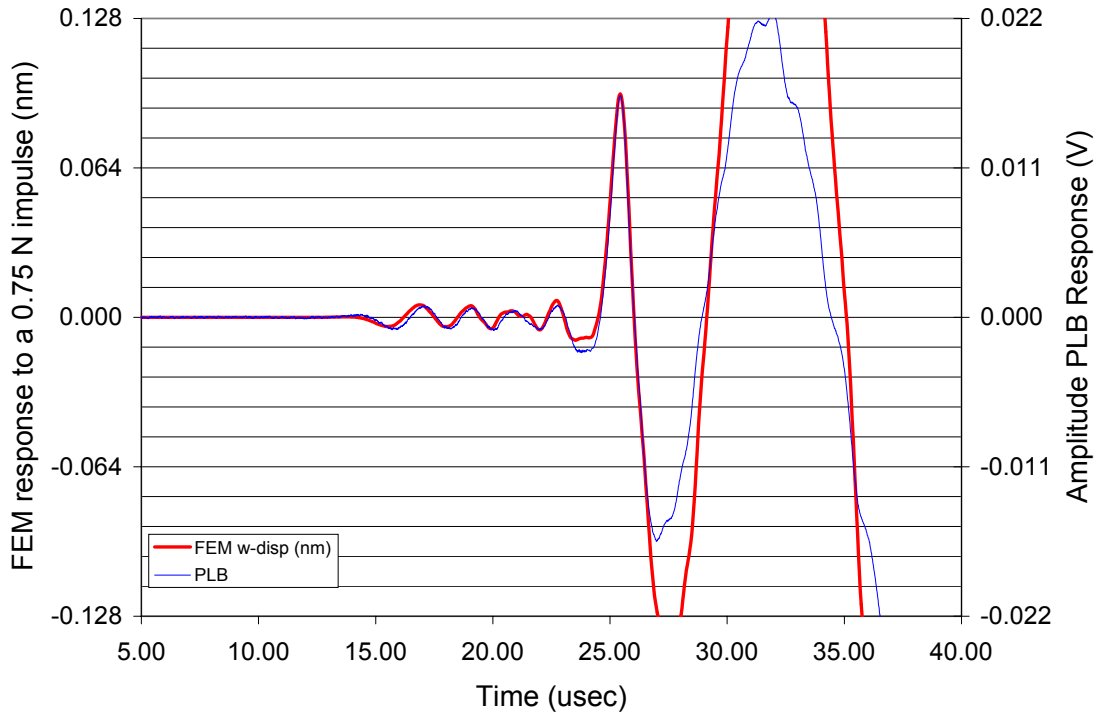


FIG. 3.5. Theory vs. experiment of PLB on aluminum plate using NIST transducer.

It seems there is a good match between the plots for the data prior to that first large peak and a significant departure after that peak. One might argue that because of the small plot size of the early peaks a small percent difference is not noticeable, but becomes very noticeable at the larger amplitudes. However, that argument falls apart when looking at the first deep valley of the PLB trace at 27 μ sec that is almost exactly the same amplitude as the first large peak. Note the significant difference with its counterpart in the FEM data.

However, assuming the FEM model is accurate, a calibration factor can be estimated for the smaller displacements using the plot scales as follows $0.022\text{V} / 0.128\text{ nm}$. The calculated value of approximately 0.172 V/nm ($1.72 \times 10^8\text{ V/m}$) is comparable to the values in the literature of approximately 1.3 to 2.0 ($\times 10^8\text{ V/m}$) for various versions of the transducer [Proctor 1982, Proctor 1986, Breckenridge 1986].

3.3 Simulated AE Experiments

An effort was made to experimentally investigate the effect of boundaries on wave propagation by doing pencil lead breaks on a set of steel specimens with increasing boundary restrictions. The first test was conducted on a steel block large enough to mimic a half space (one surface), followed by a large plate (one edge, two surfaces). The response signal was not amplified.

3.3.1 Half-space

Figures 3.6 and 3.7 are photographs of the test setup on a large block of steel. The thickness of the block is approximately 2 inches. The approximate width of the top machined surface is 3.5 inches and the bottom face 7.25 inches. It was cut lengthwise from a cylinder, hence the odd cross section. Figure 3.7 shows the wideband point contact conical transducer from NIST (brass block) inside the opened aluminum shield box. The small cylinder in the soldering stand clip to the right of the box is a small diameter piezoelectric transducer that is used as the trigger transducer for the test. Pencil lead breaks were conducted at different distances along the red magic marker line seen on top of the steel block, at 45 degrees to that line, in the direction of the transducer. The trigger transducer was kept at 0.5 inches from each PLB location; on a line perpendicular to the red line and 45 degrees from the pencil break direction.

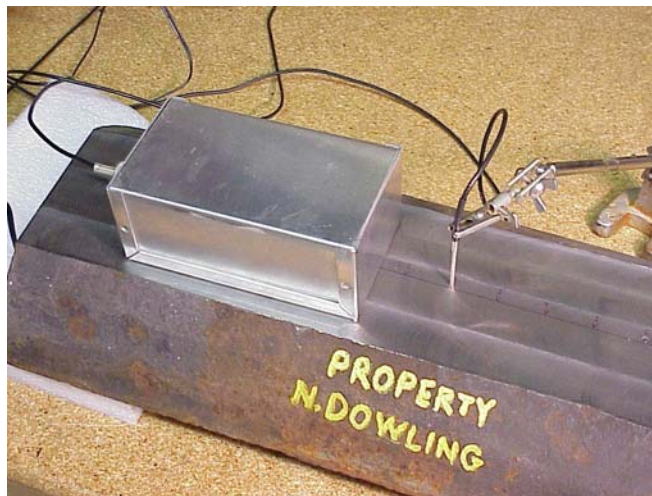


FIG. 3.6. NIST transducer setup on large steel block in Faraday shield box

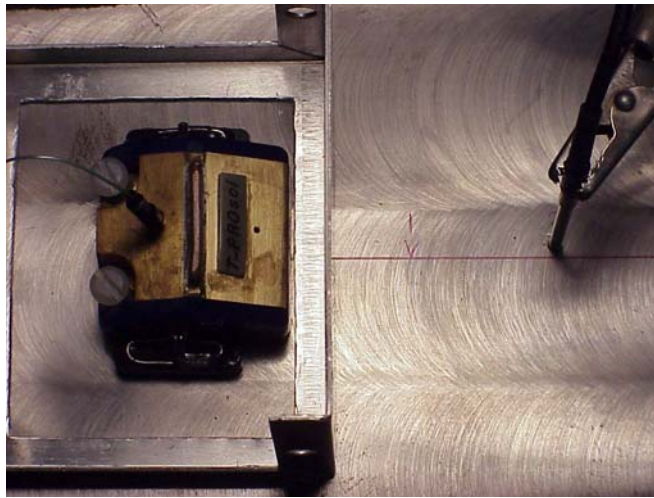


FIG. 3.7. View of NIST transducer inside of Faraday shield box

The results of that effort are plotted in figure 3.8. Each trace in the plot is the average of 5 PLB waveforms to reduce variations of the PLB source. Small inconsistencies in the trigger, on the order of tens of nanoseconds, required each original waveform to be shifted in time to line up the negative peaks of the large down-spike and not adversely affect its amplitude when averaging. However, because the trigger delay is essentially the same for each trace, the time of each negative downspike on the plot is essentially appropriate for the signal travel time minus the trigger delay. In other words, the time intervals between the spikes are appropriate to the velocity of the wave.

What is noteworthy is the amplitude reduction, with distance, of the surface wave. These distances are short enough that the primary factor in the reduction is beam spread and not attenuation due to microstructural absorption. For distances appropriate to the size of the specimens used in later tests, one should note the approximately 20-30% reduction in amplitude from the 1 inch to 2 inch travel distance. One can also calculate the velocity of the surface wave from the slope of a line fit to a plot of the arrival time of the peak versus the distance, as shown in Fig. 3.9. Therefore, the velocity is approximately $0.1176 \text{ in}/\mu\text{sec}$, which is comparable to values in the literature for steel.

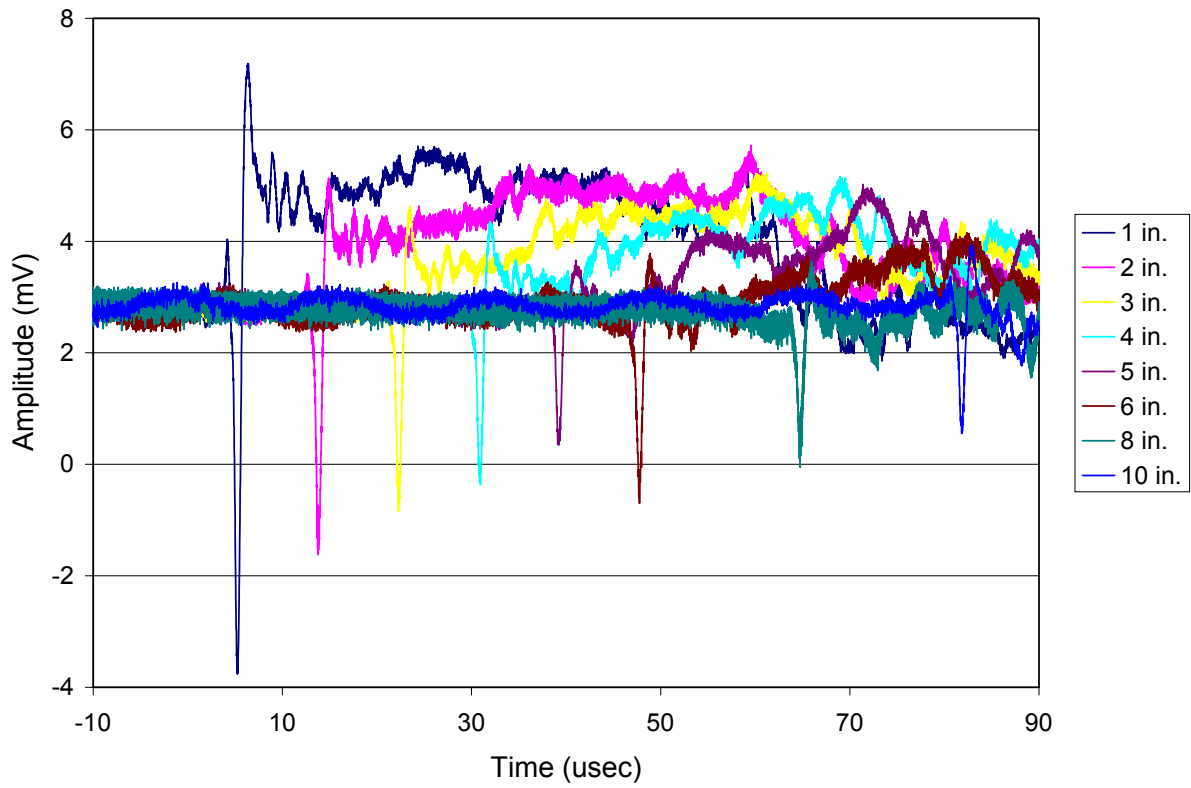


FIG 3.8. Surface wave amplitude vs. distance from PLB on large steel block

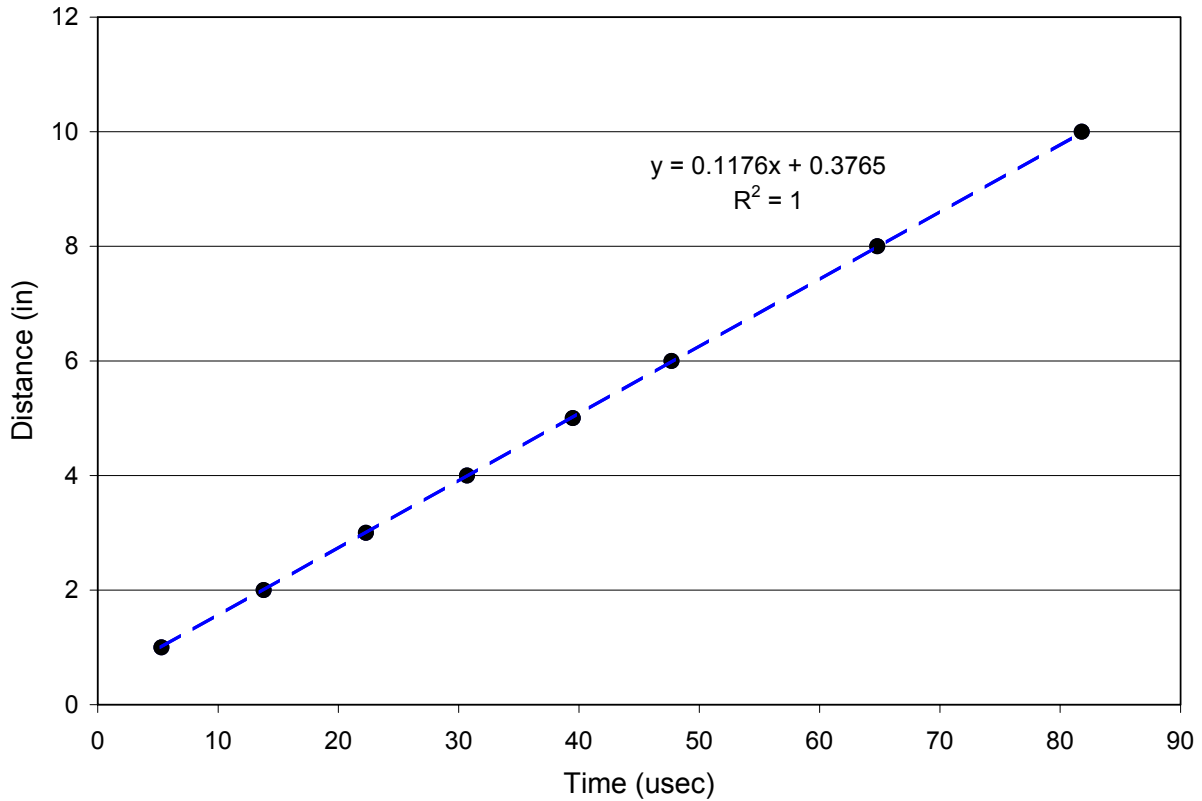


FIG. 3.9. Velocity calculation of PLB response on large steel block

3.3.2 Plate Edge

Testing PLB sources on the edge of a steel plate (approx. 18" x 5" x 0.25"), was accomplished in the manner shown in Figure 3.10. On the left end, the plate is clamped between two thick steel plates, but physically and acoustically isolated from them by two intervening drywall-sanding screens (abrasive coated mesh). The thick plates act as support for the two support screws on the transducer and a wide enough base for the aluminum shield box. Above the single C-clamp support on the right end is the soldering helper clip holding the trigger transducer with it side against the top edge of the plate. It was found that the trigger was more consistent with this configuration. The PLBs were located between trigger transducer and the NIST transducer. To maintain the same trigger delay time, the trigger transducer was kept at 1 inch away from each PLB location.



FIG. 3.10. Steel plate setup for testing PLB propagation on edge.

The results of the PLBs are shown in figure 3.11. Again, as in the previous test each trace is the average of 5 PLBs at the same location. What is extremely noteworthy is the lack of amplitude reduction of this wave. In reality, the amplitude of the spike increases, out to 4-5 inches, then seems to level off.

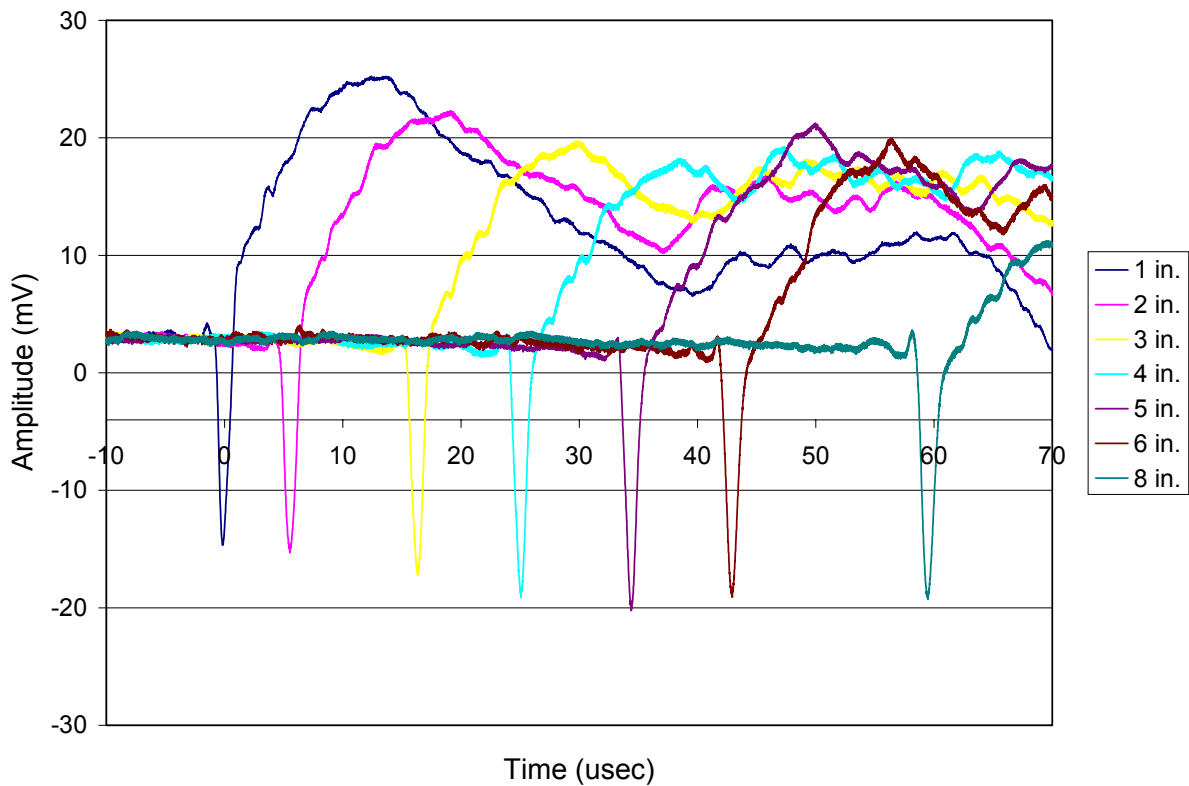


FIG. 3.11. Amplitude vs. distance from PLB on edge of steel plate

This setup with the constant trigger delay allows one to measure the velocity of the wave along the edge by plotting the distance against the time of flight, as before, and measuring the slope of a fitted line. That result is shown in figure 3.12 and the velocity of the "edge" wave is $0.1143 \text{ in}/\mu\text{sec}$.

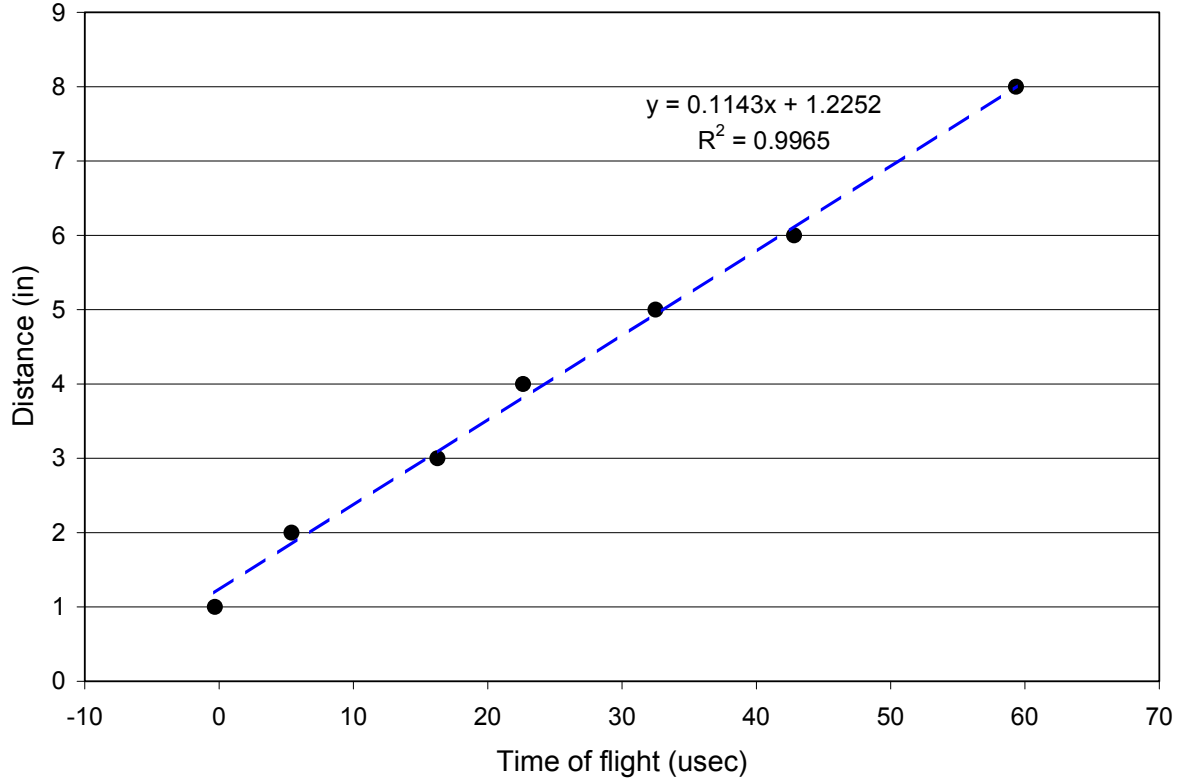


FIG. 3.12. Velocity calculation of PLB response along plate edge

How does one measure the frequency of a single surface wave spike that is a very small portion in time of the subsequent AE developed? Using a fourth order bandpass Bessel filter the frequency content of the surface wave spike due to PLB on the edge of the plate was investigated. First, the spike was filtered by setting high cutoff at the Nyquist frequency, and the low cutoff near zero. The amplitude of the spike was plotted as the low cutoff frequency was increased, essentially reducing the low frequency content. The opposite was done by setting low cutoff near zero and decreasing the high cutoff from the Nyquist frequency, again plotting the change in amplitude as the high frequencies were reduced. A plot of these amplitudes converge on a minimum amplitude around 200 kHz with the -3 dB bandwidth approximately 130-500 kHz.

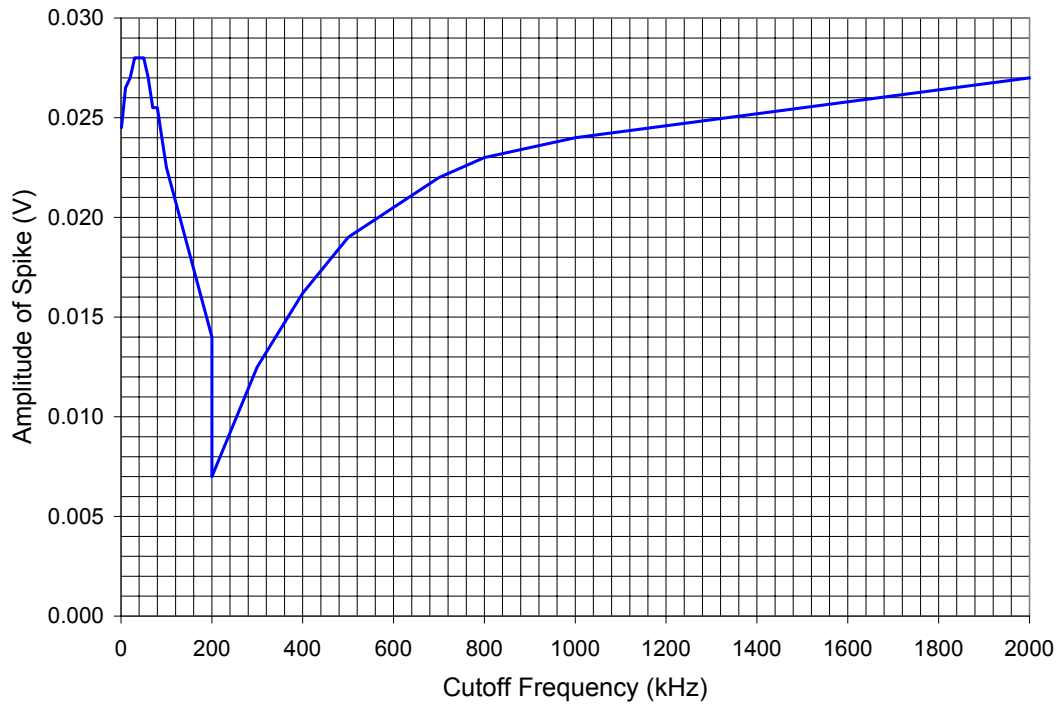


FIG. 3.13. Amplitude of PLB spike versus filtering cutoff frequency

Or one can use wavelet analysis, as described in section 2.4 in this document. The following plot of the PLB (filtered to remove large excursions below 50 kHz) shows that there is considerable content between 10 and 15 μsec , the peak being around 200 kHz amplitude and the -3 dB bandwidth ($1/1.41 * \text{max.}$ puts one into the area between yellow and green) is approximately 50-400 kHz.

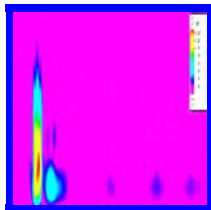


FIG. 3.14. Thumbnail: Wavelet analysis of PLB edge wave

3.4 Discussion

By combining the theoretical minimum detectable voltage at the transducer (limited by the data acquisition noise), which was shown to be approximately 0.05 mV, and the NIST transducer calibration factor of approximately 172 mV/nm, the displacement detectability during the primary experiments seems to be approximately 0.3 picometers. To put that into perspective, thermal atomic vibration at room temperature is a few picometers, unit cell dimensions for iron are approximately 300 picometers, and the Rayleigh spike displacement due to a PLB is approximately 100 picometers. In other words, if the sensor does not have a greater minimum amplitude threshold below which it is unable to sense displacement, the minimum detectable amplitude, is 0.3 picometers. Considering the NIST transducer trace in Fig. 3.5, there does not seem to be any visible jumps in the data from the baseline through the higher excursions. A jump or stair-stepping in the data greater than the noise jitter would be an indication that the sensor had a sensitivity threshold greater than the noise in the signal. Upon taking a closer look at the original acquired data, the inaccuracy of the data acquisition was determined to be approximately ± 0.25 mV because of the noise amplitude. There are no obvious jumps or stair-stepping in the original traces either, in other words, if the NIST transducer has a sensitivity threshold it was not visually resolvable within the noise of these tests. An argument could be made that since the inaccuracy of the trace is ± 0.25 mV, that the detectability is limited by that value, hence, approximately 1.5 picometers. However, an argument could also be made that, with appropriate smoothing of the data, sub-picometer detectability can be achieved. This is because the noise has apparent frequency content significantly higher than the apparent frequency of the displacement portion of the signal. Either way, it is apparent that the sensitivity of these experiments is high.

The experiments also show that the Rayleigh component of the SSP on a plate edge is initially larger than the Rayleigh component on a half-space (17 mV vs. 7 mV, respectively, after traveling 1 inch). Also, the edge propagation increases in amplitude while the half-space propagation amplitude decreases for the same distance traveled (23 mV vs. 3 mV, respectively, after traveling 5 inches). Because bulk waves traveling along the plane of the plate are restricted to spread in 2-D and similarly Rayleigh wave beam spread on a half-space is 2-D, then it is possible that the bulk wave reduction rate is possibly the same as the Rayleigh wave beam spread on a half-space. The implication is that any AE acquired on the "surface" channel that is larger than the corresponding AE on the "bulk" channel is a candidate SSP.

Chapter 4

Primary Experiments

For these experiments, the specimens used are a modified version of the standard CT specimen profile. All the specimens were polished prior to loading, and the plastic deformation at the crack tip was examined with topographical micrography techniques. The AE data acquisition for all these tests, a departure from the current typical method of acquiring AE data, captures all of the signal (emissions, background noise, quiescent times) during testing.

Tables in the appendices link to all the micrographs taken at particular stages of testing and all the waveform data plots: original, low frequency components (LF), high frequency components (HF), spectral analysis, and wavelet analysis. There are hundreds of figures linked to those tables, so the following discussions of the events for each type of steel are primarily brief summaries. In addition, the tables are coded to present other information such as the number of AE events that occurred at that particular stage of testing and what the type of failure occurred.

For the remainder of this discussion the following terms are being used. "Precracking" means the low amplitude, high frequency, fatigue cycling used to run the crack out to a designated length before the subsequent higher amplitude "overload". Two types of specimens have been tested in two different loading regimes. One is the "overload" fatigue specimen precracked to have a sharp crack tip. The other is the "plastic zone" specimen, which has been machined with a large notch in the same manner as the overload fatigue specimen, but has not been precracked prior to loading.

4.1 Specimen Design and Preparation

The specimen design primarily follows the standard compact tensile specimen profile, as per ASTM E399, except for an extended section on one leg near the lower pin loading hole as shown in Fig. 4.1. This extended section allows a transducer to sit with its contact plane parallel to the ground. The location of the active tip of each transducer is indicated by a red arrow, which incidentally is scaled very close to the actual size and shape of the tip. The location of a transducer on the extension is specifically for capturing possible surface waves traveling along the lower crack face and continuing along the notch surface. The location of the top transducer was chosen because of calculations and experimental results [Achenbach 1979, Scruby 1985] that indicate that the amplitude of the longitudinal bulk waves leaving the site of a crack tip extension event is largest in a direction normal to the crack face and lowest in a direction directly in front of the crack tip. This location also allows the transducer to sit parallel to the ground.

Another difference is that the loading clevis does not have loading flats in the pin holes to provide rolling contact between the loading pins and the clevis holes. The circular holes used are an attempt to provide a larger contact area, instead of the line contact of the loading flat on the circular pin. This lowers stress over that area, reducing the possibility of generating AE from the contact plastic deformation.

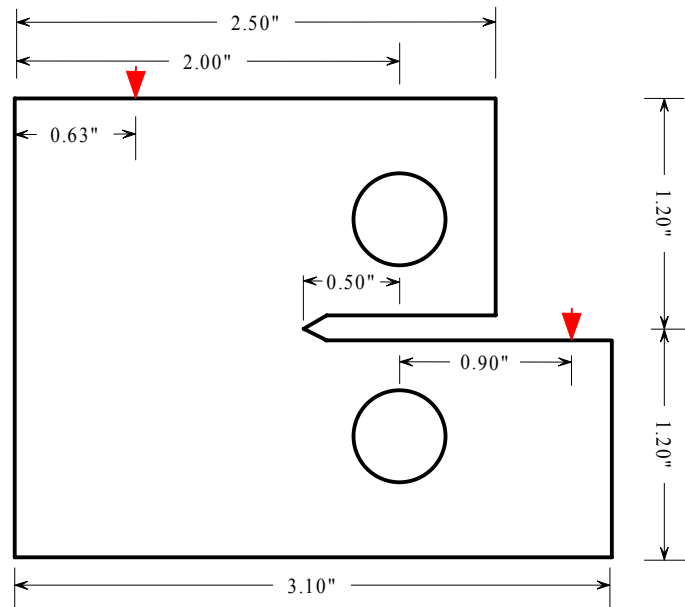


FIG. 4.1. Modified ASTM E399 compact tensile specimen profile with general dimensions.

The depth of the notch from the centerline of the pin holes to the root is 0.5 inches. Prior to any testing, one face is polished and inscribed with lines at 0.050 inch intervals for most of the specimen face. The thickness is not the prescribed dimension according to the ASTM compact

tensile specimen standard. This thickness of 0.25 inches puts the specimen in a regime between plane strain and plane stress, for all except the highest yield strength steels tested. E399 specifies that the ratio of width (the 2.00" dimension) to thickness should be in the range of 2 to 4, preferably 2. The thickness determines stress triaxiality at the tip. The thickness to ensure plane strain conditions is determined by procedures noted in ASTM E399, which also specifies that all other dimensions are functions of the thickness. The fact that they are not in plane strain (which is the worst case) is not an issue because this is an investigation of the acoustic emission behavior of steels in bridge construction or bridge design situations.

Several types of steel were used for these tests. They represent a wide range of tensile properties, and deformation behavior from very ductile to very brittle, as shown in Table 4.1. The columns marked Spec. are for values from ASTM, AISI or vendor specifications. The columns marked Test are for values from samples tested during this research. The fracture toughness values are from Barsom [1977], calculated from Charpy V-notch test values using a conversion equation in Barsom [1977], or Dowling [2003].

Table 4.1. Steel test specimen properties.

Steel type	Tensile (ksi)		Yield (ksi)		Fracture Toughness K_{Ic} (ksi $\sqrt{\text{in}}$)
	Spec.	Test	Spec.	Test	
AISI A2 ($R_c=60$)	325	200-233	NA		~ 40
AISI A2 ($R_c=50$)	240	260	NA		~ 40
ASTM A-514	110-130	117	100	110	125-200
ASTM HPS70W	85-110	91-96	70 min.	75-82	210-220
AISI C-1018	72-85		60-70		
ASTM A-588	70 min.	79	50 min.	67	> 120
ASTM A-36	58-80	72	36 min.	49	> 82

Several specimens of each type of steel were machined to the profile in Fig. 4.1. Both of the large face surfaces were hand lapped on a flat abrasive surface to remove most of the loose scale and oxidation to determine which side had the lowest extent of scratches and pits in the area along the centerline of the specimen, where the crack would run. Surface grinding of the chosen surfaces on all the specimens simultaneously produced the same thickness in the specimens. The ground faces were all finished to a metallographic polish. The following stages were chosen after consultation with the technical representative at Beuhler: water cooled 320 grit (P400) SiC abrasive coated discs, 9 micron diamond suspension, 3 micron diamond suspension, and 0.05 micron alumina suspension. Polishing of all the specimens stopped after the 3 micron diamond suspension stage and a set was picked that would produce the best surface after the final stage of polishing. Prior to any testing, the polished face was inscribed with lines at 0.050 inch intervals for most of the specimen face to measure crack advance.

Once all the machine work and polishing was finished the pin holes were preloaded to 5 kips in compression between the pin hole and the nearest appropriate edge (top or bottom outside

edge) without loading the notch. The pin holes for the specimens used for the plastic zone tests were loaded to 6 kips. A concept in NDE known as the Kaiser effect states that AE is not regenerated from a prestressed material until the stresses generated in the previous loading are reached, unless some degradation or microstructural change has occurred prior to the second loading. Hence, this procedure is to eliminate pin hole deformation AE from the overload tests.

4.2 Load Frames

Two different sets of requirements has prompted the use of two different load frames; an MTS hydraulic frame and a modified dead weight creep frame.

4.2.1 Precracking Fatigue

Precracking of the specimens was accomplished on the MTS hydraulic load frame. The extended section of the specimen precluded use of extension gauges and automatic monitoring of crack length. Even though much time was spent actively monitoring crack growth with a traveling microscope a wealth of insight was gained by continually observing the crack growth behavior. The location (of the crack tip) vs. cycle data was logged manually at intervals. Initially this was recorded for estimating the crack growth rate (da/dN) so that time spent per test could be evaluated for scheduling use of the machine. For all but the first two specimens during the first round of precracking the magnification was set so that 50 reticle graduations of the microscope corresponded to 0.050" for a theoretical accuracy of 1 thousandth of an inch (25.4 μm). The fuzziness (due to slip steps) around the crack tip (in all the specimens, worse with specimen ductility) and the motion of the image (for data recorded on the run) realistically reduced this by a factor of 3 to 5. Cycle data was recorded at best to the nearest hundred cycles, but typically to the nearest kilocycle in intervals of tens of kilocycles.

4.2.2 Overload and Plastic Zone Tests

In an effort to eliminate all potential sources of noise (for instance: machine gear and hydraulic actuator noise from powered load frames) except the AE coming from the crack the experiments were conducted on a modified dead weight load frame typically used for creep experiments. The dead weight machine is very quiet mechanically and electronically.

In addition, using a dead weight machine, for doing the overload tests, allowed the specimens to crack without load constraint. This may mimic the proper relaxation, free propagation of a crack, and dynamic load redistribution only governed by the specimen properties, such as would occur in cracks in a real structure loaded only by inertial and gravitational forces. It is questionable that the load control mode of any powered load frame (screw or hydraulic) allows the specimen to respond in the same manner, because the active control is not designed to mimic accelerations due to inertial responses. The difference between a dead weight and some type of active control, in a powered load frame, may not be sufficient to warrant this approach for mechanical property measurement, but the AE is determined by the specifics of the load redistribution and relaxation occurring at the tip, and therefore could be significantly affected.

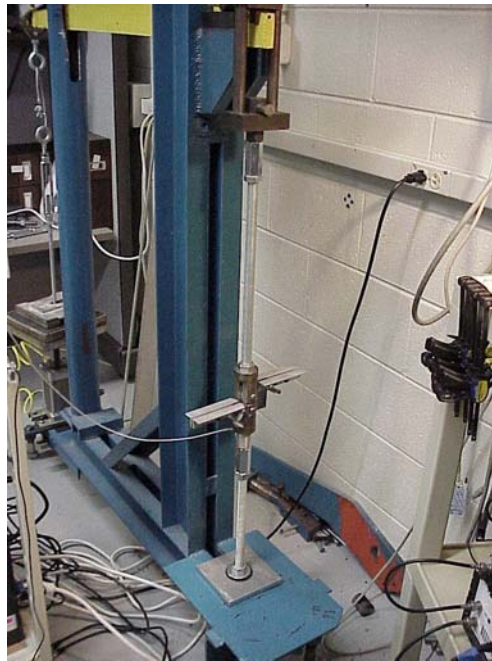


FIG. 4.2. Overall photo of Modified creep frame for overload tests

The large steel structure in Fig. 4.2, painted blue, is the modified creep frame photographed from the specimen grip end. The yellow bar at the top is a lever arm with the fulcrum only a few inches away from the centerline of the specimen. The other end holds the weight pan that has three flat rectangular cast iron weights on it.

The lever arm is set at 20:1 ratio. Hence, 100 lbs. on the "low" side weight pan creates a 2000 lbs. load in the CT specimen on the "high" side. The "low" side of the lever arm, without weights added, generates approximately 240 lbs. of preload.

Loading and unloading of the specimen is accomplished by a pneumatic actuator with a 7-inch stroke, situated under the weight pan to lift the weights. The actuator retracts faster than the weights drop, hence the loading profiles are governed primarily by gravity and inertia of the loading system. Fig. 4.3 shows the pneumatic actuator in the extended position holding up the weight pan and weights. The coiled yellow hoses are the air supply lines to the hand operated control valve, which is shown in Fig. 4.4. Electromagnetic solenoid valve control was attempted, but even with the valve shielded in a grounded steel box in a remote part of the lab, the RF generated was still affecting the data acquisition.



FIG. 4.3. Weight pan end of the modified creep frame with pneumatic actuator extended



FIG. 4.4. Manual control valve for the pneumatic actuator

The weight pan is hung from the lever arms with a steel cable loop (Fig. 4.5) so that when the weight pan is lifted up, the preload from the lever arm remains on the specimen. This will insure some crack opening prior to the overload and reduce the amount of AE from the crack surface

disparities unsticking if there was any crack closure. Both the high load side and the low load side have adjustments for length so that the frame can be returned to same geometry for each test regardless of the crack opening displacement. To monitor the load in the CT specimen a small 15 kip load cell is installed on the high load side. Reduction of noise from the metal to metal contacts of the machine parts is accomplished by applying rubber sheeting, Teflon and vinyl tape where possible as shown in Fig. 4.6. Transmission of high frequency noise from the rest of the machine to the specimen is reduced or delayed by the complexity of the shapes of the components in the load line: turnbuckles, threaded rod, cable loops. Kaiser effect is eliminated by preloading the system with a dummy (no notch) specimen in place to loads higher than the specimens are loaded.

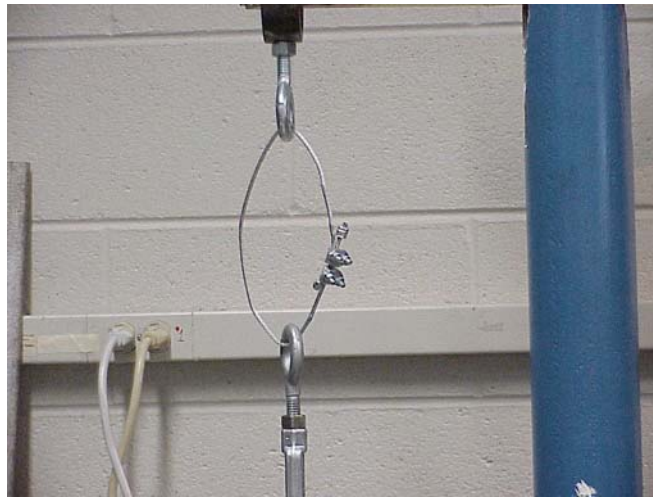


FIG. 4.5. Steel cable loop connection between weight pan and lever arm



FIG. 4.6. View of one of the degree of freedom fulcrums with rubber pad installed

The load signal was monitored during tests run with the dummy specimen under several appropriate different loads to characterize the behavior of the loading mechanism. The load cell signal is also used as the external trigger signal for the data acquisition. This allowed consistency of triggering and comparable timing between the different tests. Since the precracking occurred at 1 kip the data acquisition was not triggered until 1 kip was reached, again because it was thought Kaiser effect was valid. Typical load profiles are shown in Fig. 4.7. It is interesting to note that the system elasticity allows vibration to occur around the peak static load level. The plots cover the same time interval that the data acquisition system can gather data during the actual experiments. Note that the peak load occurs around 0.10 sec for the most of the overloads (50 lbs. of weight was used up to and including overload 10). At overload 11, the weight was increased (to 60 lbs.) to increase the stress intensity, instead of substantially increasing the crack length. Overload 12 used 70 lbs., overload 13 used 80 lbs. and overload 14 used 90 lbs., creating a high side load increase, between overloads, of approximately 200 lbs.

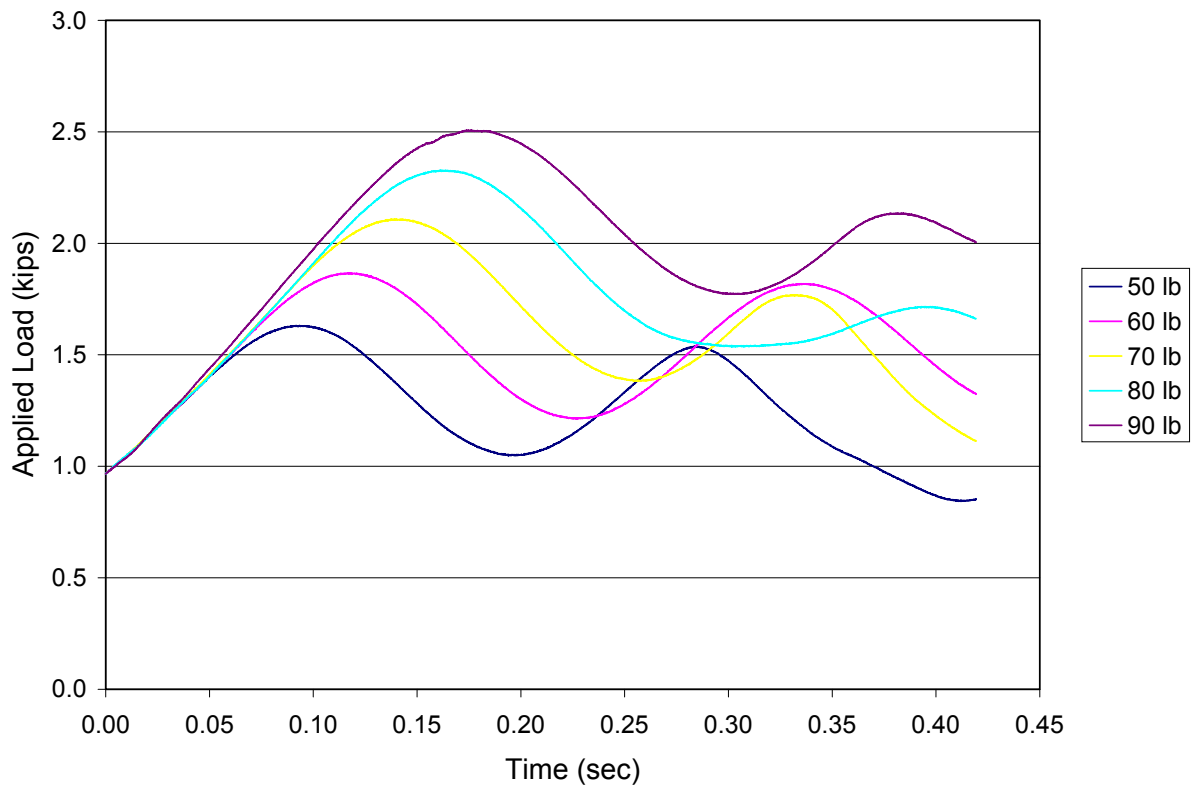


FIG. 4.7. Load profiles vs. weights applied

Each of these profiles is an average of three runs. Note the consistency of shape up to the first trough. The variation between the profiles after that point is due to the variations in time of the actuator extension (load reduction) by the hand controlled valve. It was felt that the variation was a minor issue because of Kaiser effect.

4.3 Instrumentation

4.3.1 Preamplifiers

Most AE systems use preamplifiers between the transducer and the data acquisition instrumentation, typically as close in the signal path to the transducer as possible, to boost the signal for travel back long lines to data acquisition electronics. The original idea for this research was to avoid using preamplifiers, to reduce the amount of noise generating circuitry in the signal path. However, this policy changed after the noise tests, as discussed in Section 3.1.2, supported the concept that, for this situation, detectability could improve, with amplification.

4.3.2 Transducer Setup

The transducers used are the same NIST design transducers discussed earlier. Figures 4.8 and 4.9 show the installation of the transducer support arms and the shield boxes on a specimen in the load frame. Alignment marks were used to help keep the transducers located in the same position from run to run. Clips with rubber bands holding the transducers and clamps holding the shield boxes eliminated movement during loading. Even though it is hard to see in the figures, proper alignment meant keeping the support arms and shield boxes from direct contact with the clevises. The cylinder below the clevises with a white cable extending from it is the load cell.



FIG. 4.8. Specimen installed in load clevises with transducer support arms attached



FIG. 4.9. Specimen installation with Faraday shield boxes installed

4.3.3 Data Acquisition

A similar setup as described for the preliminary experiments was used to monitor the AE. The primary difference is the use of the Gage data acquisition board with the 16-bit amplitude resolution and 10 MHz maximum sampling rate. The amount of onboard memory, as previously mentioned, allowed approximately 0.41 sec of uninterrupted data acquisition at a sampling rate of 10 MHz.

4.4 Data Reduction and Analysis

4.4.1 Data Reduction Procedure

After a specimen was installed in the testing machine and all the NIST transducers were attached, just prior to loading the response of both channels to PLBs on the specimen was recorded. This was primarily to check if all connections and electronics were secure and working. However, either the quiescent portion of this recorded data (the PLB activity was a small fraction of the entire record) or data from a separate set of records acquired when nothing was happening to the specimen was used as a noise sample. These noise samples were considered a typical compilation of all possible ambient noise sources (ambient RF, RF from all the electronics, environmental acoustic, etc.) at the time of the each experiment.

The method used to acquire the "AE" data record is a digital analogue of the concept of turning on a tape recorder and capturing "everything". By triggering the data acquisition at a particular load (using the signal from an in-line load cell for the trigger signal) all the activity seen by the transducers was recorded regardless of the amplitude, for a portion of time limited only by the amount of dedicated high-speed memory on the data acquisition board. The amount of memory available allowed approximately 0.4 second long records for sampling rates of 10 Megasamples/sec for a total of 4 million data points per channel.

The first cut at data "analysis" occurred just after acquiring the data. The Gagescope software that controls the data acquisition hardware offers a very capable digital oscilloscope display that allows the acquired data to be viewed with different time base and amplitude scales from all the channels simultaneously. After every acquisition, a review of the signals was performed at a large time base to show "all" the data at once. Since each record has 4 million data points, it is impossible to display every single point at those scales. The software accommodates by reducing the number of actual data points displayed to the number of available screen pixels (decimation) in one of two methods: mean, where the mean of the data in each small interval is shown to represent that interval, or min-max; where the minimum and maximum values in an interval are shown. Min-max was the mode used when doing all visual scanning of the data because large excursions are retained. This allowed one to note areas of interest, scroll to those points and zoom in, magnifying the data record to a point where there was no decimation. This approach quickly showed that the data seemed to have high frequency content modulated on, at times, a much larger amplitude low frequency excursion, making it very difficult to even decide what areas to choose for further detailed frequency analysis. Since the low frequency excursions occurred typically throughout the entire record, it was very time consuming to do visual inspection of the record.

Samples of the data were analyzed using several different methods. Several programs were written implementing various types of analysis: spectrum analysis, moving (or boxcar) averaging, filtering (Bessel and Butterworth IIR filtering), enveloping (magnitude of analytic signal) [Gammel 1984], and deconvolution. Although many of these techniques may provide valuable insight when used on small samples, they became unworkable in dealing with the data

set as a whole. A relatively fast way to review the data set and mark the areas of interest was needed.

It was discovered that the signals did indeed have three distinct frequency bands. To many AE researchers this will not be surprising. It has been promoted that the large amplitude frequencies below 50 kHz should be filtered out because they included structural resonances, which do not provide important information. Traditionally "AE" falls into the 100 to 500 kHz band, while frequencies above 1 MHz are filtered out because they are felt to often be noise, due to the electronics, RF interference, etc. For these experiments, "AE" does seem to be falling into the 100 to 500 kHz band. It was also determined that the frequencies above 1 MHz did not provide pertinent information. Several samples from these experiments indicate that significant energy does exist in frequencies below 15 kHz. However, the issue may be that those frequencies do have information regarding the state of the damage.

In the subroutine libraries of programming environments such as Mathematica, Matlab, Labview, there are digital implementations of classical analog filters such as Chebychev, Butterworth, or Bessel, available for use by the programmer. Hence, they are very attractive to investigators familiar with the mathematics of the analog versions, and are useful in many situations. However, they fall into a class of filters [Hayes 1999] called infinite impulse response (IIR) filters. Even though there are varieties of IIR filters that have minimum phase distortion, none have zero phase distortion. In other words, any phase delay created by the filter is a function of frequency. So, different frequency components of the original signal have different delays in the output relative to the input. Another class of filters, finite impulse response (FIR) filters, have linear phase distortion, where the coefficient of the exponential on the phase component of the magnitude-phase representation of the frequency response of the filter is a constant, i.e. delay is not a function of frequency. Hence, all frequencies have the same delay. Therefore synchronizing events or features in the original signal with the resultants in the filtered signal is a simple matter of deleting a set number of data points in the output, determined by the filter parameters being used, as will be discussed later.

The following time domain analysis procedure that was developed and found to be very effective and efficient on the large 4 Megasample records. Each entire record was low-pass filtered using a moving average filter. The resultant, the low frequency portion of the original time data, was adjusted for any time delay introduced by the filter. It was then subtracted, point-by-point, from the original record. Since the original data tended to be high frequency information modulated on a low frequency baseline, this step resulted in the zero-baselined high frequency portion of the signal. This was then subjected to low pass filtering (with a much higher breakpoint than the previous filter stage) to eliminate very high frequency RF noise in the signal.

The filtering stages used a simple algorithm called a boxcar moving average, also known as a smoothing filter. It performs by creating a new data point that is the equal weighted average of a certain number of data points surrounding the corresponding data point in the original data set. The window then shifts forward one point on the original data set and does a new average to create the next point. It is called a boxcar average because the weighting window is rectangular, i.e., all coefficients which multiply the points in the original data set are equal. It is very efficient on very large data sets because it operates in the time domain, and has the added advantage of

being an FIR filter. The time delay or phase shift between input and output is $\frac{n-1}{2}$ elements, n being the number (preferably odd) of coefficients in the averaging window. So synchronizing the output data set with the input is a simple matter of eliminating the first $\frac{n-1}{2}$ data points.

The programs used to implement the mentioned data analysis method were written in LabView, a visual data flow programming language. Documentation of these programs is in Appendix B. Those not familiar with LabView will be surprised to see images similar to the front panel of electronic instrumentation and electronic schematic diagrams instead of lines and lines of program code. Much discussion could be had about LabView programming and its advantages and disadvantages. However, in the simplest terms, instead of having lines and lines of textual commands (code), compiled and executed or interpreted to manipulate numbers and control equipment (as in other programming languages), one draws images/pictures/schematics (visual code) that when "executed" (interpreted) can also manipulate numbers and control equipment. Therefore, the documentation is not lines and lines of code, it is mostly pictures.

The program (ViewPeakDetectSig.vi) reads the binary format data files created by the data acquisition software (Gagescope) directly; there is no need to convert to a much larger and cumbersome ASCII format. 4 Megasample/ 8 Mbytes binary format records typically increase space requirements 12 X to 25 X when converted to ASCII format files, depending on whether a time column is included. The signal is separated into its high and low frequency components, as previously described, which are saved into individual Gagescope format files. This allows viewing with the Gagescope software. The filtering stages are user adjustable for the number of coefficients used. After testing various window sizes on some 10 Megasample/sec data, it was decided to set the first stage to 167 points and the second stage to 7 points. This created, in the first stage, a low pass filter that rolled off to zero at 60 kHz with a small ripple above that frequency. The second stage significantly reduced frequencies above 1.4 MHz. Rectifying and thresholding the high frequency data, creates a third "peak marker" file. The excursions above a threshold value (peak markers) are saved with the same location (in time) and amplitude of the data in the original high frequency data set; all other data being zero. The threshold value was calculated as the mean plus a certain number of standard deviations of a sample of the corresponding noise data for each channel and experiment. The mean was always essentially zero, and it was found that a value of 4.5 standard deviations reduced the number of threshold crossings to a workable level without eliminating AE events.

The other documented VI (ViewSpectSig) reads Gagescope signal files and plots the magnitude spectrum. Statistics are performed on the signal and the data is saved to an ASCII spreadsheet file. The other programs are SubVI's (subprograms in LabView parlance), used in the primary data analysis programs noted above, and "tool" programs used during the creation of the programming that can read and write the binary format Gagescope data files.

4.4.2 Determination of Seismic Surface Pulse Criteria

To determine if a particular event on channel 1 was a seismic surface pulse (SSP) running along the crack face from the tip, several criteria were developed and are discussed in the following paragraphs:

- Velocity: Different modes of wave propagation have different velocities, so using that information and the geometry of the specimen, the time delay between the channel 2 and channel 1 signal of the arrival of different combinations of waves (from the same event), can be determined,
- Amplitude: Wave propagation characteristics allow us to estimate the relative amplitudes between the channel 1 and channel 2 signals,
- Frequency response profile vs. time: Wavelet analysis of selected events can determine the relative amplitudes and arrival times of content of different frequency,
- Shape of the time domain signal: PLB responses have been shown to have front edge characteristics different from the subsequent displacements.

Velocity

One can calculate the arrival times of various types of wave propagation from an AE source at the crack tip to the locations of the two NIST transducers in an effort to distinguish between the modes. Using the experimentally derived velocity of the "surface wave" on the edge of a plate as discussed in section 3.3.2 for surface disturbance traveling along crack surface from crack tip to NIST on lip one can calculate the arrival times and subsequently the delay between them.

By ray tracing on the geometry of the specimens one can see some possibilities of wave impingement at the transducer locations. Figure 4.10 shows selected ray traces for all the different overload crack lengths. The crack length a is measured from the line connecting the center of the pin holes to the blue dot that represents the crack tip location (the crack is not drawn in the schematics). The blue and green lines show the direction of waves leaving a possible source at the crack tip. They were drawn showing the possibility of direct impingement or direct reflection (1 bounce). If a direct reflection was not possible due to the shadowing by the pin hole then the nearest path past the pin hole was drawn. The red lines are the like-mode reflections i.e. longitudinal. Since an understanding of the early arrival history at the transducer is needed, the initial approach is to first consider only longitudinal waves. Mode conversion, upon reflecting (the orange lines), to the slower shear mode of propagation will obviously show up later.

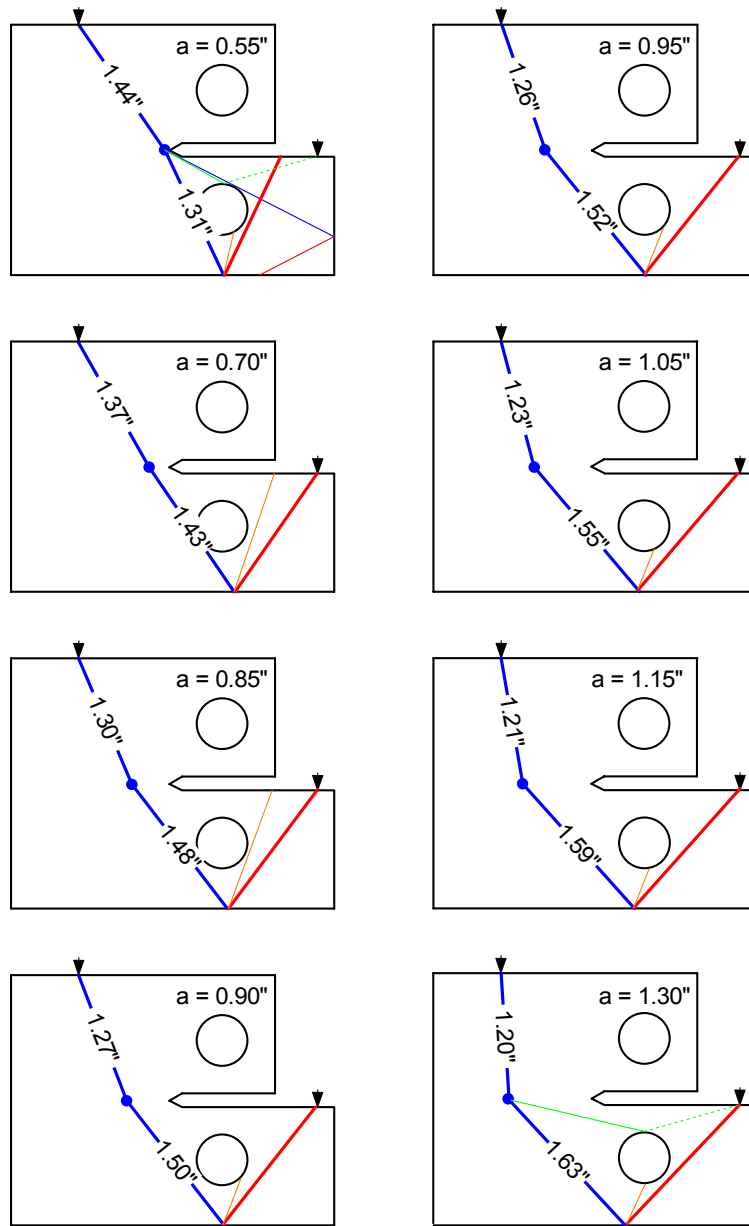


FIG. 4.10. Determination of AE signal history at different crack lengths.

The first noteworthy observation is that the pin hole provides a significant amount of shadowing of the lower transducer ("surface wave" transducer and data acquisition channel 1) on the specimen extension from waves in the bulk of the specimen. At overload 1 ($a = 0.55$ "), no direct reflection can make it to the surface wave transducer. Almost everything making it past the topside of the pin is reflected down and away, back into the body and only a small aperture is

available for wave travel below the pin hole into the extension. However, direct reflections can occur at the longer crack lengths.

The green lines show the low grazing angle at the pin hole where the amount of reflected energy toward the surface wave transducer is small because of the dispersion of the circular surface. The low incident angle at the transducer indicates that the particle displacement direction for the longitudinal reflection is almost perpendicular to the axis of the transducer, the primary direction of sensitivity. Therefore, those two factors should leave any indication on channel 1 to be very small.

Calculating the time delay between several possible modes from the same source traveling to the surface wave transducer (channel 1) and the fastest (longitudinal) to the upper transducer ("bulk wave" transducer and data acquisition channel 2) is shown in figure 4.11. The legend codes L, R, S, and F stand for longitudinal, Rayleigh, shear, and reflected longitudinal, respectively. The numbers are the channel number. The red trace is the surface wave component of the seismic surface pulse on channel 1 versus the longitudinal on channel 2. The blue and green lines are the delays for the head of longitudinal and shear waves running along the crack face. Only the shear head wave will have particle displacement in the sensitivity direction of the transducer, but the notch width (shape) itself possibly shadows the transducer from both of those head waves. The yellow is the longitudinal reflection from the bottom surface of the specimen towards the surface wave transducer.

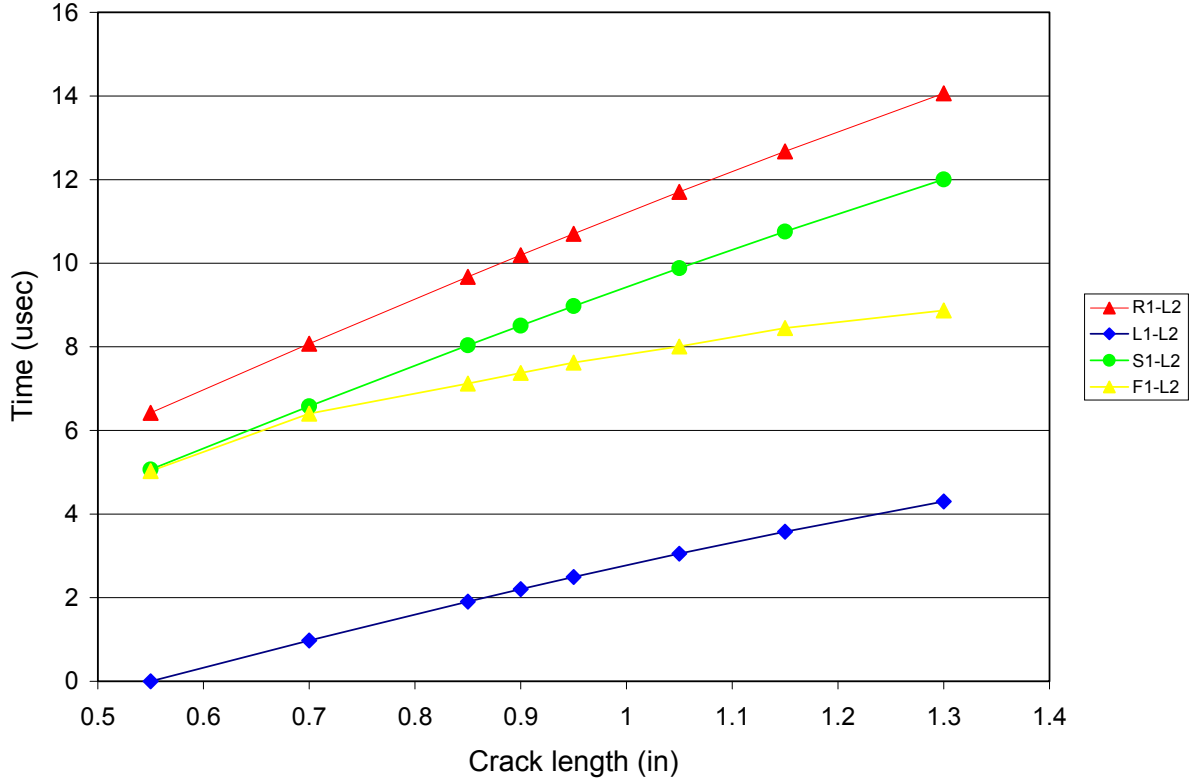


FIG. 4.11. Calculated time delay between signals on channel 1 and channel 2. R = Rayleigh, L = longitudinal, S = shear, F = reflected longitudinal

Amplitude

Calculations (and comparison to experimental results) [Bruttomesso et al 1997, Budaev and Bogoy 1995] show, respectively, that a surface wave crossing an 150 degree convex corner (angle in the material) has a transmission coefficient of 0.931 and one crossing a 210 concave (angle in the material) has one of approximately 0.60. So the amplitude of a surface pulse crossing both drops to 0.55 of the original. A surface wave, leaving the crack tip of the specimens used in this experiment, has to cross those two angles of the notch before reaching the transducer. However, this calculation should only be used as an estimate, because the propagation is on the edge of a plate, and the calculations were done for corners in a half-space.

Even with the reduction, it is felt that the channel 1 AE data should show higher amplitude than the amplitude for the corresponding event on channel two. AE propagation leaving the tip heading for the channel 2 transducer is constrained to expand in only two dimensions, as are Rayleigh surface waves on a half space (even though there are no constraining boundaries, the characteristics of the wave propagation allow no net energy loss into the half-space). Therefore

the reduction of amplitude due to radiation expansion is expected to be on the same order as the PLB response on a "half-space" (section 3.3.1). The surface wave propagation running along the crack faces towards the channel 1 transducer, as a guided wave (as experimentally noted in 3.3.2) should exhibit less reduction (also noted in 3.3.2) over channel 2 signal (which should have reduction analogous to that in 3.3.1). The 45% losses, noted above, could be taken into account, but we do not know what are the starting amplitudes of the various modes of wave propagation at the crack tip. As noted in a previous chapter, for normal excitation on a half space, 67% of the energy is partitioned into the surface wave component of the response and less than 7% into the longitudinal. Admittedly, the issue is that this situation is not a half-space, but the edge of a plate. However, unless the proportions are dramatically different for the edge propagation, the larger starting amplitude of the surface wave more than compensates for the losses.

Frequency profile vs. time

Figures 4.12 and 4.13 show the time-frequency profile of a PLB on the edge of a plate compared to the time-frequency profile of an AE event from a brittle running fracture. The first is the PLB response passed through the same filtering as all the results for this research. The last is an event from the catastrophic fracture of the A2 ($R_c=60$) specimen. Note that after filtering the PLB does have some features similar to the brittle AE event such as early short duration high frequency content followed by lower frequency content. However, some differences are also apparent. The high frequency content for the AE is centered around 500 kHz with a smaller peak around 200 kHz, while the PLB high is around 200 kHz with some 500 kHz content. It is very possible that although the PLB does generate the seismic surface pulse, the pencil lead fracture is slower than the AE event in the steel. Therefore, a longer impulse, when the steel under the PLB unloads, and lower frequency content.

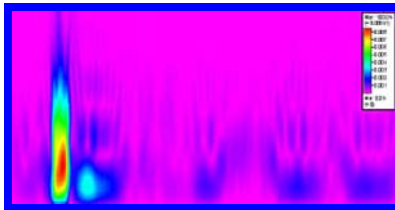


FIG. 4.12. Thumbnail: Wavelet plot of filtered PLB on plate edge

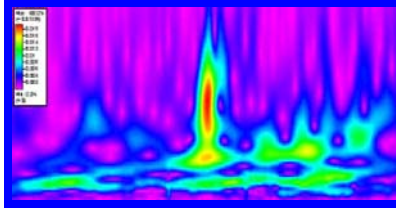


FIG. 4.13. Thumbnail: Wavelet plot of A2 ($R_c=60$) event from rapid brittle failure

Time domain shape

Shape of the time domain waveform could be argued as being subjective. The main issue is the possible lack of a calibration signal to compare the AE to. Also because the PLB response is from a different stress state than the SSP; the rapid release of a compression load on a surface vs. the response to a release of tensile loading at the crack tip, the shape of the time domain waveform may be different, or at least inverted. However it is felt that the prime characteristic of an early rapid rise time single cycle followed by lower frequency content can be used to at least sort out the possibilities.

4.5 Test Procedure

Many setup "helpers", such as tapered pins and large machined flat surfaces, were used to maintain alignment consistency of fixtures and speed up specimen installation. It was much easier and more consistent to clamp the transducer support arms onto the specimen prior to installation in the machine, and the transducer and shield boxes after. Utilizing a large block of aluminum with machined surfaces, the surfaces of the support arms and the specimen that the contact points of the transducer rested on, were maintained coplanar as the clamps were tightened. During installation of the specimen into the machine, the tapered pin was inserted through one arm of the clevis, catching a plastic spacer washer, through the specimen pin hole, catching another spacer washer on the other side, and finally through the other arm of the clevis. The loading pin was then used to push out the tapered pin, which maintained all those parts in alignment during the loading pin insertion. The loading pins had registration marks on one end at the periphery to allow registration of the pins in the same orientation for all the tests. The pins and clevises had all been preloaded before the tests to eliminate contact deformation AE.

A registration mark made on the load frame allowed adjustments in the load line to bring the load arm back to the same starting geometry regardless of the amount of crack opening induced at a previous stage. The only time an adjustment was not implemented was between the repetitions for the overloads where multiple repetitions occurred.

For each set of tests (either the plastic zone tests or each of the overloads), all the specimens were run during the same test session, to reduce the need to rebalance the load cell electronics during a set, once all the adjustments were made prior to the set. Micrographs were taken of the specimens before and after each set of tests. The precracking fatigue was conducted between the "after" pictures of the previous overload and the "before" pictures of the subsequent overload.

4.6 Plastic Zone Tests

4.6.1 Load Regime

To distinguish between plastic zone "AE" and crack extension AE, a set of specimens, that had been machined with the notch but had not been precracked, was loaded while monitoring AE. These tests are also a negative test of the seismic surface pulse criteria, because it is considered unlikely that plastic zone formation events distributed around the tip have the right characteristics to generate SSPs. The more ductile types of steel: A36, 1018, A588, HPS70 and A514 were used for these specimens. As seen in the figure 4.14 of the load profile for these tests, the time to the peak load (approx. 5 kips) is longer than the overload test load profiles, hence the data acquisition sampling rate had to be reduced from 10 MHz to 5 MHz to capture the peak. Therefore, the total time for each record is approximately 0.8 sec. This lower sampling rate also introduces the possibility of aliasing the results because the Nyquist frequency of 2.5 MHz is much closer to the "traditional" range of AE frequencies. However that possibly will not be a problem since the resonance that we think is due to plastic zone formation is on the order of Hz.

(As a reminder, tables in the appendices link to all the micrographs and all the waveform data plots: original, low frequency components (LF), high frequency components (HF), spectral analysis, and wavelet analysis.)

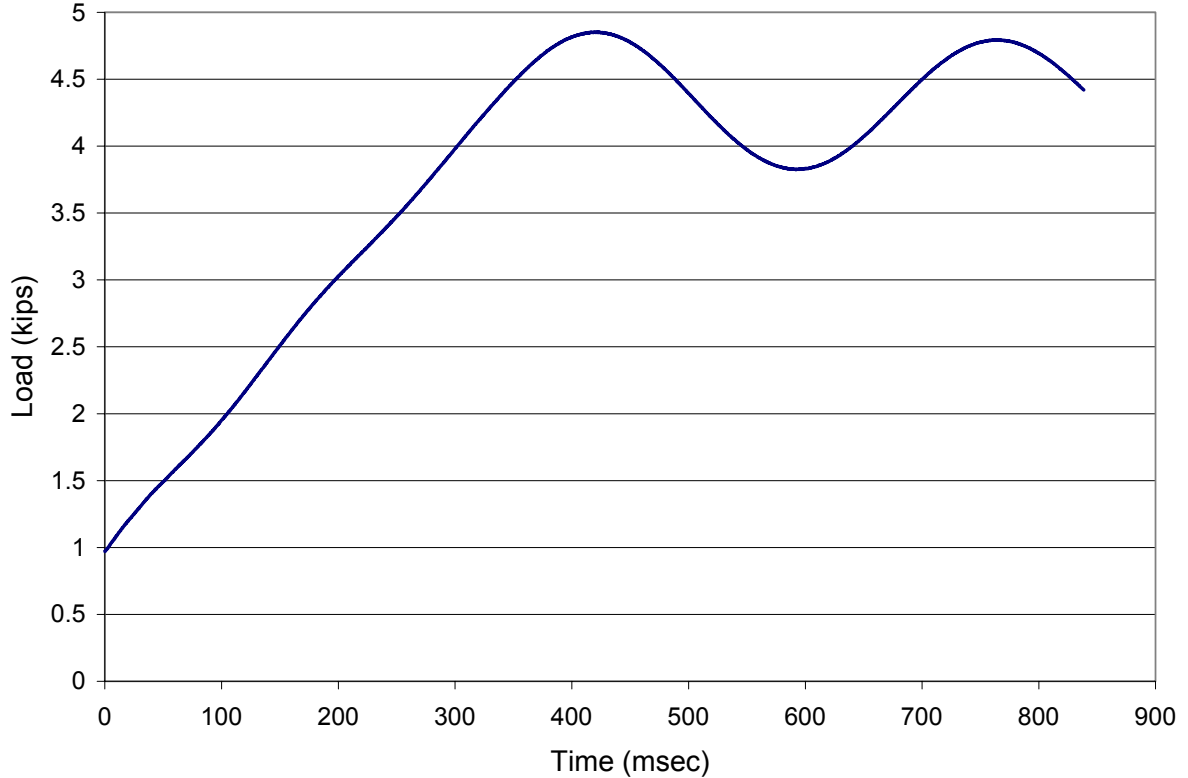


FIG. 4.14. Load profile for plastic zone tests

4.6.2 Results and Discussion

AE

The only plastic zone specimen that has possible AE in the channel 1 high frequency data is the A36 specimen. The only specimen that has no events in the channel 2 high frequency data is the HPS70 specimen. All the other specimens essentially have nothing in channel 1 and a few events in channel 2. This trend seems to fit the thought that plastic zone formation (predominantly a conglomeration of many microstructural events occurring distributed around the crack tip) emits most of its AE as bulk modes of wave propagation, because the surface wave generation at the tip requires discrete rapid crack development and extension events right near the crack surface.

Micrographs

There is no obvious crack development near the tip of the notch of the A36 specimen, but there is much deformation in the specimen. The AE on channel 1 could be attributed to the proclivity to twin as evident in the micrographs in Fig. 4.15, showing slip surface deformation extending from the notch over to and around the pin holes. Evident from their location, if these events emitted AE, the channel 1 transducer would pick it up.

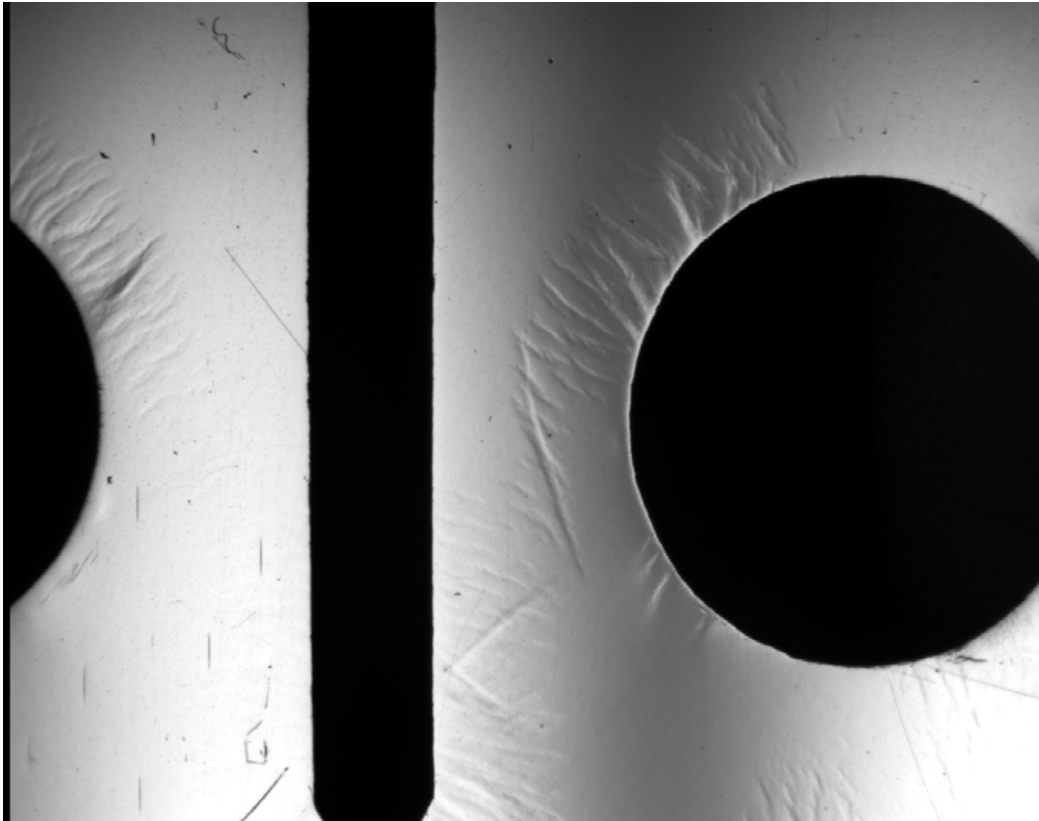


FIG. 4.15. Surface deformation of the A36 plastic zone specimen with 0.125" wide notch and 0.5" diameter pin holes.

For the other specimens there are some indications in the micrographs of strain localization near the tip. It is currently unknown whether they are cracks. The most likely candidates for cracks are the 1018 and the A514 specimens.

Consideration of Seismic Surface Pulse Criteria

The A36 events are eliminated because it is very likely that they came from the deformation around the pin hole.

Velocity: As noted there is no localization in most of the channel 1 data so one cannot even decide when, if any, content exists.

Amplitude: The scales of the time domain plots, except the A36 specimen, indicate all channel 1 events were less than or equal to the amplitude of the corresponding event in channel 2. The channel 1 "events" are essentially background noise level.

Frequency profile: In general, the seismic surface pulse profile can be characterized loosely as early localized high frequency content on channel 1. For these tests, the only events that show any high frequency content on channel 1 are from the A36 specimen.

Shape: As before; no local content, therefore no "shape".

In summary, none of the criteria for a seismic surface pulse is supported, therefore, it seems that the plastic zone tests support the idea that plastic zone formation at the tip does not produce any surface waves along the crack face (in this case, just the machined notch face).

4.7 Overload Tests

4.7.1 Load Regime and Precracking

The loading scheme for the overload specimens is indicated in figure 4.16 that is a plot of stress intensity due to load versus crack length for standard CT profile specimens. "Precracking" fatigue to run crack tip to the next overload location was carried out with a load cycling regime of 50 to 1000 lbs. as indicated by the "1 kip" curve or an $R = P_{min}/P_{max} = 0.05$. The maximum stress intensity for each overload is indicated by the labeled symbols. Each different symbol is due to the load peak of the loading profile. Note that overloads 3, 4, and 5 were carried out at approximately the same crack length with only 1 kilocycle of precracking fatigue between them. Overloads 10-14 were also conducted at approximately the same crack length with 50 cycles of precracking fatigue between them, except for 100 cycles post-overload 10 (pre-overload 11). A preload due to the 0.24 kip weight of the lever arm itself is not indicated. Overloads 1-4 were single cycles, so calling the lever arm preload a condition of minimum stress intensity is a misnomer because the specimen was loaded from 0 to K_{max} , albeit in 2 stages. However, for Overloads 5 and 6, 5 cycles were conducted from preload to maximum load (K_{min} - K_{max}) without removing the specimen from the machine, but rearming data acquisition and acquiring data each time. In addition, a result of the loading procedure is that there are several cycles of a few hundred pounds that is called a "single" overload. Because of the quick scan of the results Overloads 7, 8, 9 were conducted slightly differently. Multiple "single" cycles were conducted until something other than low frequency resonance occurred, then one more cycle was conducted, up to 5. This saved some time and effort, but, unfortunately this and the fact that the precracking amounts were determined by distance instead of a set number of cycles, does not provide each specimen with the same load history.

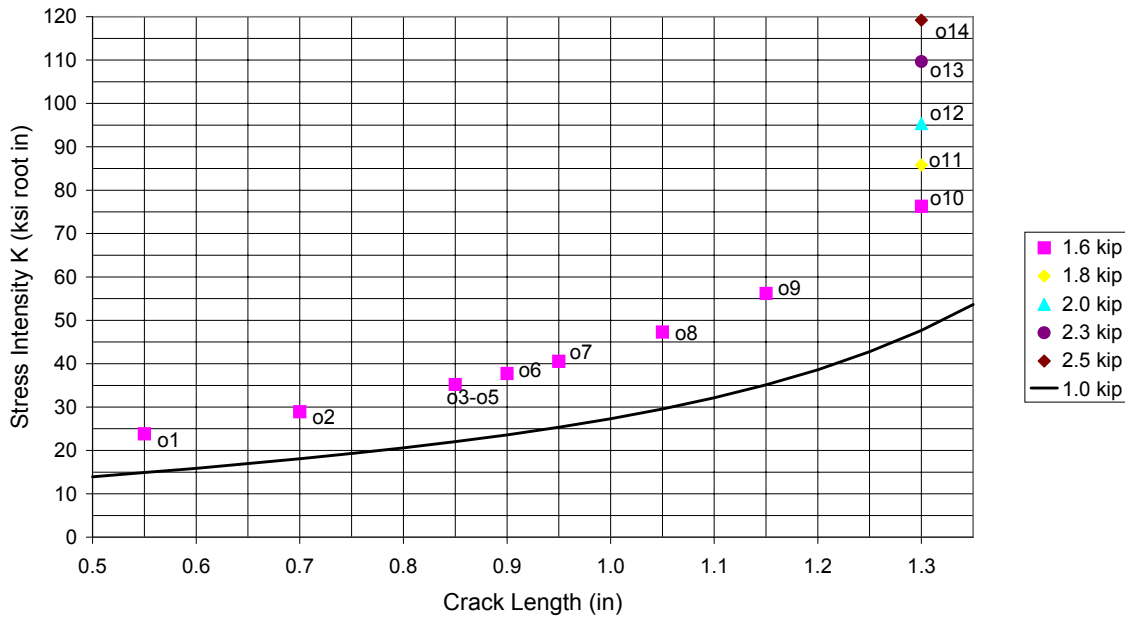


FIG. 4.16. Stress intensity progression during load regime with preload and overloads 1-14

Several failure load calculations were used to guide the development of the load regime: fracture toughness, nominal yield, and plastic limit load failure criteria presented by Dowling [1977]. The concept was to approach failure by starting with a load and crack length estimated to not promote failure of any type, and then increase crack length. At the point when failures of the ductile specimens started occurring (1.3 inch crack length), it was decided to hold crack length constant (except for small increments of precracking fatigue), and increase the load. The "ductile" specimens (all except hardened A2 steel, see Table 4.1) fall in a range of yield strengths from 50 to 100 ksi. For the overload value of 1.6 kips, nominal yield was not expected to occur for the 50 ksi specimen until a crack length of 0.9 inches was reached. Plastic limit load failure for that specimen and load should occur at about 1.2 inches. Admittedly, the nominal yield failure equation does not take into account the stress intensity at the tip. If the stress intensity at the tip is high enough the failure can be governed by fracture toughness. The lowest fracture toughness of the ductile specimens of approximately $80 \text{ ksi}\sqrt{\text{in}}$ should fail with a 1.6 kip load at a little over 1.3 inches, whereas "completely brittle" specimen failures (approximately $40 \text{ ksi}\sqrt{\text{in}}$) should fail under 1.6 kip at a little over 0.9 inches. As is noted in the tables in the appendices that is approximately what happened. The specimens started failing by plastic limit (when tensile plastic zone met compressive plastic zone) at the crack length of 1.3 inches, in order of increasing yield strength as the peak load was increased, except for the hardest

specimens. Those specimens failed in brittle fracture at crack lengths of 0.70 and 0.85 inches (25 and 30 ksi $\sqrt{\text{in}}$, respectively).

4.7.2 Results and Discussion

Before presenting results for specific steels, a few general comments can be made. Only the A2 specimens failed with a brittle running crack failure, at low stress intensity. The other specimens failed in "nearly" fully plastic yielding (plastic hinge failure) in rank of decreasing ductility: the A36 failing first and the A514 actually not failing at the last overload. "Nearly" is a description related to the way the failure process for all the ductile failure overloads progressed. Because of the plastic hinge, the resistance by the specimens never peaked and the weight pan followed the actuator retraction and subsequent extension. Fortunately, the preload weight of the lever arm was not enough to continue the deformation and the arm never bottomed on any parts of the load frame and therefore did not create unwanted AE. Hence, the load profiles noted above are not valid for these failure overloads and the specimens were not pulled completely apart, but do have significant crack mouth opening displacements. However, for the specimen overloads that were not failures, nearly all the AE occurred in the period of the load profiles up to the first peak.

(As a reminder tables in the appendices link to all the micrographs and all the waveform data plots: original, low frequency components (LF), high frequency components (HF), spectral analysis, and wavelet analysis.)

A36

This is the least brittle of the all the steels tested. Overload 1 has one high frequency (HF) event. The next event is a very large late event (at 331 ms) occurring at overload 6 rep 4. The low frequency component of this "event" is very large, nearly 1 V. The two high frequency indications, one on each channel, are more than 15 μsec apart and therefore are possibly not due to the same event. There are no more HF events until overload 8. Several occurred during repetition 1 and 1 during repetition 2. All the channel 2 data is significantly bigger than its counterpart in channel 1. Overload 9 has more events occurring than overload 8. Overload 10, the failure load (plastic hinge failure) has a very large amount similar to the ones in the plastic zone tests. All overload 10 channel 2 data is larger than counterpart in channel 1 except for event 318. Essentially no events are considered to be an SSP.

1018

There is no HF AE until the plastic hinge failure at overload 10 with only one event. This event is a very good candidate for being an SSP as indicated in the following comments and illustrated in figure 4.17.

Velocity: It is obvious that channel 2 is leading channel 1. Looking at the first large negative peaks in the time signal or the zero crossings following those peaks, which correspond well

with two of the red peaks in the wavelet plot, the delay is approximately 13-14 μsec . That fits very well with the theoretical delay for that crack length presented previously.

Amplitude: The time scales fit to the time signals or the amplitude of the first negative pulse show that channel 1 amplitude is greater than channel 2.

Frequency profile: The time-frequency plot for channel 1 is less conclusive. It has early localized high frequency, however there is some low frequency even earlier. However the duration does not seem to be as long as in channel 2.

Shape: The time-domain shape of the event on channel 1 does lead with a higher amplitude high frequency single cycle that does fit the shape criteria.

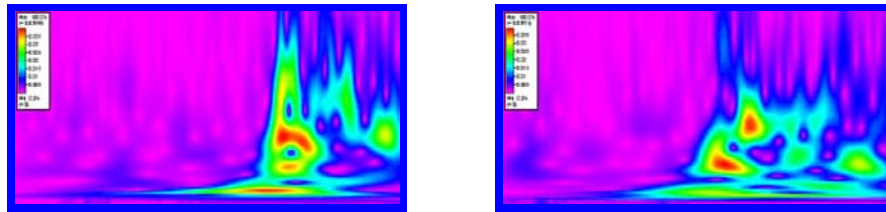


FIG. 4.17. Thumbnails: Wavelet plots of 1018o10 AE event: channels 1 and 2.

A588

There seems to be no appreciable AE events for the A588 specimens. Even the failure overload (11) is extremely quiet. The only thing that stands out is a low frequency tone-burst event from overload 7 repetition 1. The HF component of overloads prior to overload 9 have the characteristic of a "constant" background, in other words the standard deviation of the "background" on that scale is constant for the entire record. The later overloads have some slightly "bulgy" sections approximately 50-100 msec long where it seems the standard deviation would be larger, except for the failure overload 11.

HPS70

There are AE events for overloads 1, 2, 5 repetition 1, 7 repetition 1, 8 repetition 3 and 12 (the failure overload) for a total less than 20 events. The amplitude in channel 1 of the events in overload 1 are 3 times greater than in channel 2. For overloads 5 and 7 the amplitudes are comparable and for overloads 8 and 12 there are no obvious events on channel 1. The characteristics of 8 and 12 are also different from the others. The overloads prior to overload 9 have the characteristic of discrete AE events approximately 1-2 msec long on a "constant" background, in other words the standard deviation on that scale is constant for the entire record.

The later overloads have some slightly "bulgy" sections approximately 50-100 msec long where it seems the standard deviation would be larger.

A514

There are 2 AE events in overload 1. One seems to be plastic zone related (no obvious AE in channel 1) and the other, at 38 msec, is a candidate SSP. Overload 2 at first seems to have many possibilities for AE. However, upon closer examination they, except one, are residuals left over from possible RF noise spikes with very high amplitudes that were not completely filtered out. Overload 3 has a few events. There are single events in overload 4 and overload 6 rep 1. Several events each occur in overloads 9, 11, and 13. Of all the events only three show any possibility of being SSPs by having some moderately localized HF content in the channel 1 data. They are shown in figures 4.18 - 4.20.

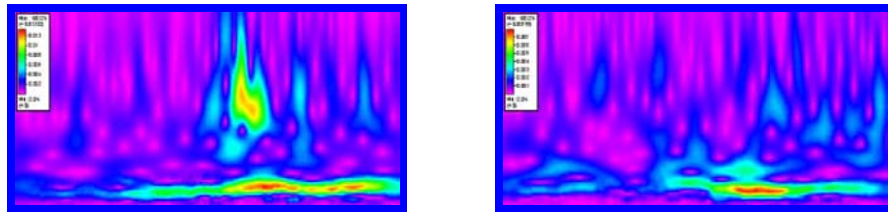


FIG. 4.18. Thumbnails: Wavelet plots of A514 overload 1 event 038: channels 1 and 2.

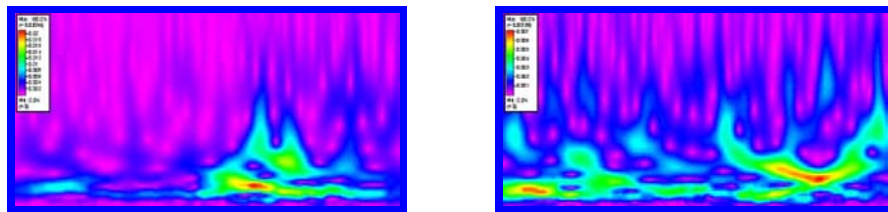


FIG. 4.19. Thumbnails: Wavelet plots of A514 overload 4 event 022: channels 1 and 2.

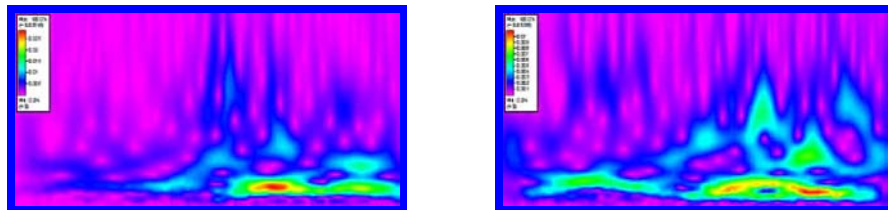


FIG. 4.20. Thumbnails: Wavelet plots of A514 overload 9 rep 1 event 024: ch. 1 and 2.

Consider the SSP criteria for the noted events.

Velocity: There is very little localizing in channel 2 so a distinct arrival time is not easily decided. However, a low frequency peak of approximately 100 kHz is arriving approximately the same time for both channels in the overload 1 event.

Amplitude: The scales of the time domain plots indicate the amplitude of all channel 1 events were greater than the amplitude of the channel 2 events.

Frequency profile: The seismic surface pulse profile can be characterized loosely as early localized high frequency content on channel 1. There seems to some early HF content, the most evident in the overload 1 event.

Shape: There is no distinct early large amplitude single cycle HF followed by lower frequency on channel 1.

All the other events had no localized event on channel 1, essentially just background noise of lower amplitude than channel 2. The "bulgy" sections, like those mentioned above for the HPS70, start showing up in the overload 7 channel 2 HF data.

A2 ($R_c=50$)

Of all the steels tested, the two A2 specimens exhibit almost completely brittle behavior. This is obvious because the failure stress intensity for both was less than $40 \text{ ksi}\sqrt{\text{in}}$. Because of that, they were considered "calibration specimens" because they were expected to generate SSP, especially during the brittle failure. The A2 ($R_c=50$) specimen has a little more toughness because it is tempered to a lower hardness. It failed at overload 3 ($30 \text{ ksi}\sqrt{\text{in}}$).

There are a significant number of events for all the overloads, but only the early occurring events (for each overload) were extracted from the data, because of they are relatively far apart in time and not likely to be reflections.

The time-frequency plots in figure 4.21 are of an event chosen to be from a condition as far from rapid brittle fracture as possible (for the A2 specimens). It is an early event from overload 1. The arrival time of channel 1 is relatively easy to decide from either the time domain signal plot or the wavelet plot. Consider either the first large peak, in this case negative, as are all the events for this and the A2 ($R_c=60$) specimen, or the highest amplitude frequency content (red area at 200 kHz), both are at approximately $255 \mu\text{sec}$. Channel 2 is almost impossible to decide arrival time from the time domain plot because of the low amplitude energy spread over time and frequency. However, it can be noted that there is a time-frequency peak of 200 kHz that occurs at $250 \mu\text{sec}$. A delay of $5 \mu\text{sec}$ is plausible for an SSP but it fits better to the head portion of a shear wave traveling along the crack face. However, the question is, does the amplitude on channel 1 of over twice that of channel 2 fit with a shear head wave?

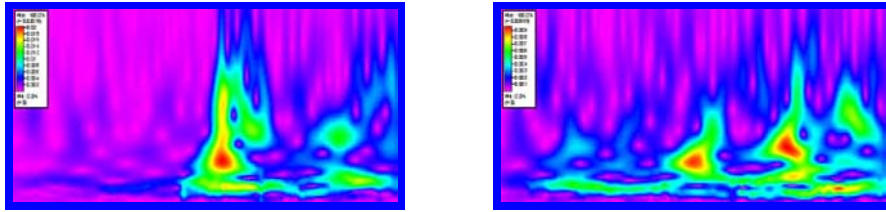


FIG. 4.21. Thumbnails: Wavelet plot of A2 ($R_c=50$) overload 1 AE event: ch. 1 and 2.

A2 ($R_c=60$)

This was the most brittle specimen of the set. It also only lasted to the second overload (25 $\text{ksi}\sqrt{\text{in}}$) before failing in rapid fracture. Many events occurred in both overloads, but only the early occurring events (for each overload) were extracted from the data, because of they are relatively far apart in time and not likely to be reflections. The larger density of later events, hence possible interference between events, makes identification difficult.

The high frequency component of the signal shows events increasing in amplitude with time, peaking around the peak load for overload 1. The amplitudes on channel 1 are approximately 2 times the amplitudes of channel 2. Micrographs show at least 80 μm of crack extension with possible bifurcation for that overload.

Overload 2 is a rapid complete fracture with very large amplitude events significantly larger than overload 1. Again, channel 1 has larger amplitude than channel 2. One of following time-frequency plots has been presented earlier as comparison to a PLB response and is shown again in the set of figure 4.22. This was because it was an event from a brittle rapid failure as is the AE in the research noted in Section 1.4 (that promoted the idea of Rayleigh wave generation for running crack propagation). Therefore, it was considered to be a "calibration specimen".

Consider the SSP criteria.

Velocity: Using the same approach as previously in the 1018 and A2 ($R_c=50$) sections, the first largest negative peak in channel 1 occurs almost exactly at 250 μsec . The "first largest negative peak" in channel 2 is not as easily identified. If the reader agrees that the one at approximately 244 μsec is it, then the lead of 6 μsec is close to the calculation that channel 2 should lead channel 1 by about 8 μsec for SSP validation. However, it does fit better with the 6-7 μsec delay for a shear head wave on channel 1 vs. longitudinal on channel 2.

Amplitude: By any measure the amplitude of channel 1 is significantly larger than channel 2.

Frequency profile: The time frequency profile for channel 1 is distinctly early localized high frequency followed by lower frequency longer duration content.

Shape: The shape of the time domain signal is also definitely an early arrival of a large amplitude single cycle very similar to the PLB responses presented earlier. Other

characteristics of the shape may not seem similar but that may be, again, because of the issue of PLBs being compression release responses while a rapid crack extension may be a tension release response.

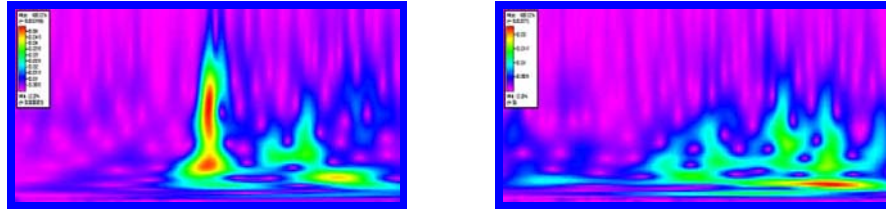


FIG. 4.22. Thumbnails: Wavelet plot of A2 ($R_c=60$) overload 2 AE event: ch. 1 and 2

4.8 Summary of Results

Plastic zone formation, considered an unwanted secondary source of AE, was found to not produce any wave propagation resembling the SSP. Therefore, it did not interfere with the SSP activity. Non-catastrophic crack extension deformation in the more brittle material during fatigue can create surface displacements resembling a seismic surface pulse. Other investigators have only demonstrated existence during monotonic tension catastrophic fracture. The overload results demonstrate the existence of wave propagation on the crack surfaces with 2-3 times the amplitude of the corresponding bulk waves, confirming the concept presented previously in the first contribution. One interesting result, for the HPS70 steel, is that the channel 1 amplitude started out with the high amplitude at the shorter crack length and decreased as the crack length increased. Crack surface displacements resembling a surface seismic pulse did occur during ductile failure.

Chapter 5

Closure

5.1 Discussion

This research has been ostensibly to investigate the existence of Rayleigh wave generation in near-failure fatigue. However to pick one phenomenon, out of the crowd, so to speak, requires an understanding of the other possibilities. Therefore, in reality, this has been an exercise in trying to understand all of the near-failure microstructural phenomenon and how they generate acoustic emission.

To review some abbreviations and terminology:

AE - Acoustic emission, section 1.2.5.

SSP - Seismic surface pulse, section 2.1.1.

PLB - pencil lead break, section 3.2.2.

"surface" channel - data acquisition channel and transducer location, section 4.1.

"bulk" channel - data acquisition channel and transducer location, section 4.1.

precrack - high frequency, "low" load fatigue regime, chapter 4 introduction.

overload - short duration, 1-3 cycles, high load regime, chapter 4 introduction.

plastic zone - describes specimens and tests with no crack extension, chapter 4 introduction.

To reiterate:

A few concepts were presented in chapter 1. AE is the most appropriate method for assessing the state of a crack. Rayleigh wave AE possibly exists on crack faces. Also, ductile sources emit AE of less amplitude than brittle mechanisms. These implied that specimen design needed to allow access to the possible Rayleigh waves, noise and secondary sources as discussed in 1.3.5 needed to be eliminated, and AE monitoring sensitivity needed to be high.

The highlight of chapter 2 is that there is research that indicates, measured normal to the surface, that the Rayleigh component of the SSP starts out at least 10 times the amplitude of the longitudinal wave component. The displacement of the longitudinal wave in the direction of propagation (in this case perpendicular to the surface) is approximately 3.4 times (for steel) the transverse displacement. Hence, the initial amplitude of the Rayleigh component, as measured by the surface wave transducer, is at least 3 times the amplitude of the longitudinal component measured in the direction of propagation, as measured by the bulk wave transducer.

Experiments presented in chapter 3 show that the experimental equipment can detect picometer displacements. To put that into perspective, thermal atomic vibration at room temperature is a few picometers, unit cell dimensions for iron are approximately 300 picometers, and the Rayleigh spike displacement due to a PLB is approximately 100 picometers.

Also, the Rayleigh component of the SSP on a plate edge is initially larger than the Rayleigh component on a half-space. The edge propagation increases in amplitude, up to a point, while the half-space propagation amplitude decreases for the same distance traveled. Because bulk waves traveling along the plane of the plate are restricted to spread in 2-D and similarly Rayleigh wave beam spread on a half-space is 2-D, then it is possible that the bulk wave reduction rate is the

same as the Rayleigh wave beam spread on a half-space. The implication is that any AE acquired on the "surface" channel that is larger than the corresponding AE on the "bulk" channel is a candidate SSP.

The primary experiments of monitoring AE during plastic zone formation and overloading were presented in chapter 4. A summary of the test results is shown in Table 5.1

Table 5.1. Summary of AE tests.

	Steel Type (in order of increasing yield strength)						
Test ↓	A36	1018	A588	HPS70	A514	A2, R50	A2, R60
Plastic Zone	ACB	AC2	AC2		AC2		
Overload 1				#3S	#2S	#4S	#4S
Overload 2				#4S	#1S	#4S	FB #4L
Overload 3					#4S	FB #5L	
Overload 4					#1S		
Overload 5				#1S			
Overload 6	#2S				#1S		
Overload 7			#1?	#1S			
Overload 8	#6S			#2S			
Overload 9	#8S				#4S		
Overload 10	FP #8L	FP #1S					
Overload 11			FP #0		#2S		
Overload 12				FP #1S			
Overload 13					#3S		
Overload 14							
<p>Code legend: FP = Failure by Plastic Hinge FB = Failure by Brittle Fracture #0 = No AE in high frequency (HF) component #nS = n HF events analyzed, typically all the possible events in that test #nL = n sample of HF events analyzed from a large group (>>20) ACB = AE both channels, AC2 = AE channel 2 only</p>							

Out of 62 overload tests only 25 have what may be considered AE. It is obvious from the table that the AE events are sparse and not evenly distributed among the tests. The 1018 and A588 specimens generated essentially no AE during overload.

In summary, very sensitive AE tests were conducted during overload conditions. These conditions were considered to be the best for provoking significant crack extension thought to generate AE of any kind. There were emissions that fall into the category of possible Rayleigh waves generated by crack extension. However, just being able to say the previous statement based on experimental evidence may be important regardless of whether the mode is a Rayleigh surface wave or not. This was a unique effort to record with high fidelity and classify different modes of wave propagation, by shape and "instantaneous" frequency content, from sampling two transducers simultaneously on a specimen shape that helps to differentiate the modes.

5.2 Accomplishments

- The possibility of surface modes of AE wave propagation generated from crack extension events was illustrated using an idealized thought experiment. These modes have much higher amplitudes than bulk modes.
- Investigation of the several aspects of AE monitoring in finite objects showed that:

Surface wave propagation on an edge of a plate is larger and degrades less than surface wave propagation on a half space and bulk wave propagation,

The NIST conical transducer and the data acquisition instrumentation have high fidelity and the ability to detect picometer displacements,

"Standard" AE calibration sources (pencil lead breaks) were shown to be consistent and much larger than the AE events they were simulating,

Brittle AE events have higher frequency content than PLBs.

- Criteria were devised based on velocity, frequency content, amplitude and shape to determine if an AE event is a seismic surface pulse, which has a prominent Rayleigh surface wave component.
- A unique testing paradigm was devised with the following features to reduce interference from secondary sources of AE and enhance the investigation of AE from increasingly critical crack propagation:

Extended section of a compact tensile specimen profile allowing sensor access to surface wave propagation,

Two channels of simultaneous, synchronized data acquisition that can monitor AE uninterrupted for the duration of the loading regimes,

Cable support of the weight pan on a dead weight load frame allowing lever arm preloading of the specimen during tests, mimicking loading conditions in large steel structures like bridges, and reducing AE due to crack closure and unsticking,

Time domain filtering and frequency partitioning software developed for assessing large digital AE data files with 4 million data points.

5.3 Conclusions

- The lack of sufficient AE distributed throughout the test regime did not allow for a general determination of conclusive changes in the AE as the specimens approached failure. Therefore, these particular tests were unable to track criticality.
- Plastic zone formation, considered an unwanted secondary source of AE, was found to not produce any wave propagation resembling the SSP. Therefore, it did not interfere with the SSP activity.
- Overload tests that generated crack surface displacements resembling a surface seismic pulse showed that it does have larger amplitude than the bulk wave AE.
- Non-catastrophic crack extension deformation in the more brittle material during fatigue can create surface displacements resembling a seismic surface pulse. Other investigators have only demonstrated existence during monotonic tension catastrophic fracture.
- Crack surface displacements resembling a surface seismic pulse can occur during ductile failure.

5.4 Recommendations

- In a sense, this research was conducted in the least hostile crack growth environment. Conditions of room temperature and dry air are least likely to instigate AE from brittle behavior. Many infrastructure failures have been exacerbated by extraordinary conditions such as cold (ductile-brittle transition), corrosive environments (stress corrosion cracking) and other conditions (hydrogen embrittlement). The test paradigm developed in this study should be used to study the crack growth process under these hostile conditions.
- Alternative specimen profiles and loading regimes to increase tip stress intensity at much longer uncracked ligament lengths should be considered.
- Further data mining directed at correlating AE features with crack morphology should be explored, as well as consideration of the spectral analysis of the low frequency content.

References

- Achenbach, J. D., K. Hirashima, and K. Ono. (1983). "Acoustic Emission Due to Nucleation of a Microcrack in the Proximity of a Macrocrack." *Journal of Sound and Vibration*, 89(4), 523-532.
- Achenbach, J. D., and Harris, J. (1979). "Acoustic Emission from a Brief Crack Propagation Event." *Journal of Applied Mechanics*, 46, 107-112.
- Amzallag, C. (1994). "Automation in Fatigue and Fracture: Testing and Analysis." ASTM STP 1231, American Society for Testing and Materials.
- Barsom, J. M., and Novak, S. R. (1977). "Subcritical Crack Growth and Fracture of Bridge Steels." NCHRP Report 181, Transportation Research Board, Washington D.C.
- Beevers, C. J. (1980). "The Measurement of Crack Length and Shape During Fracture and Fatigue." L. Engineering Materials Advisory Services, ed., Chameleon, London.
- Boyer, H. E., ed. (1975). "Failure Analysis and Prevention." Metals Handbook, 10, American Society for Metals, Ohio.
- Breckenridge, F. R., Proctor, T. M., Hsu, N. N., and Eitzen, D. G. (1986). "Some Notions Concerning the Behavior of Transducers." *Progress in Acoustic Emission*, 675-684.
- Bruttomesso, D. A., Jacobs, L. J., and Fielder, C. (1997). "Experimental and Numerical Investigation of the Interaction of Rayleigh Surface Waves with Corners." *Journal Of Nondestructive Evaluation*, 16(1), 21-30.
- Budaev, B. V., and Bogy, D. B. (1995). "Rayleigh Wave Scattering by a Wedge." *Wave Motion*, 22, 239-257.
- De Vadder, D., Park, Y., and Francois, D. (1995). "Apparatus for Ultrasonic In Situ Accurate Crack Size Measurement on Laboratory Test Specimens." Special Applications and Advanced Techniques for Crack Size Determination, J. J. Ruschau and J. K. Donald, eds., American Society for Testing and Materials, Philadelphia, 114-129.
- Debnath, L. (2002). *Wavelet Transforms and their Applications*, Birkhäuser, Boston.
- Donald, J. K., and Ruschau, J. (1991). "Direct Current Potential Difference Fatigue Crack Measurement Techniques." Fatigue Crack Measurement: Techniques and Applications, K. J. Marsh, R. A. Smith, and R. O. Ritchie, eds., Chameleon, London, 12.

- Dowling, N. E. (1977). "Fatigue-Crack Growth Rate Testing at High Stress Intensities." *Flaw Growth and Fracture*, 139-158.
- Dowling, N. E. (1993). *Mechanical Behavior of Materials*, Prentice-Hall, New Jersey.
- Dowling, N. E. (2003). Dissertation discussion with M. R. Horne. Blacksburg.
- Duke, J., J. C., Sison, M., and Horne, M. R. (1996). "Acoustic Emission Monitoring of Steel Bridge Members." *Contract No. 0569-010*, Virginia Tech, Blacksburg.
- Dunegan, H. L. (1987). "Typical Acoustic Emission Signal Amplitudes Expected from Primary Mechanisms responsible for Failure of Pressure Vessels, Piping, Tanks and Valves." #8709, Dunegan Engineering Consultants, Inc.
- Enoki, M., and Kishi, T. (1991). "Development and Future Aspects in AE Source Characterization." *Acoustic Emission: Current Practice and Future Directions*, W.
- Sachse, J. Roget, and K. Yamaguchi, eds., American Society for Testing and Materials, Philadelphia.
- Fleck, N. A. (1991). "Compliance Methods for Measurement of Crack Length." *Fatigue Crack Measurement: Techniques and Applications*, K. J. Marsh, R. A. Smith, and R. O. Ritchie, eds., Chameleon, London, 69-93.
- Gammell, P. M. (1984). "Coherent Processing of the Full Analytic Signal Information of Ultrasonic Waveforms." *International Advances in Nondestructive Testing*, 10, 183-266.
- Hayes, M. H. (1999). "Digital Signal processing." *Schaum's Outline*, B. Gilson, ed., McGraw-Hill.
- Jenkins, P. J., and Briggs, G. A. D. (1991). "Acoustic Microscopy." *Fatigue Crack Measurement: Techniques and Applications*, K. J. Marsh, R. A. Smith, and R. O. Ritchie, eds., Chameleon, London.
- Kamath, S. M., and Kim, K. S. (1986). "On Rayleigh Wave Emissions in Brittle Fracture." *International Journal of Fracture*, 31, R57-R62.
- Karpur, P., et al. (1995). "Nondestructive Crack Size and Interfacial Degradation Evaluation in the Metal Matrix Composites Using Ultrasonic Microscopy." *Crack Size Determination*, J. J. Ruschau and J. K. Donald, eds., American Society for Testing and Materials, Philadelphia.
- Khan, Z., Rauf, A., and Younas, M. (1997). "Prediction of Fatigue Crack Propagation Life in Notched Members under Variable Amplitude Loading." *Journal of Materials Engineering and Performance*, 6(3), 365-373.

- Lindley, T. C., and McCartney, L. N. (1981). "Mechanics and Mechanisms of Fatigue Crack Growth." *Developments in Fracture Mechanics*, G. G. Chell, ed., Applied Science Publishers, London, 247-322.
- Marsh, K. J., Smith, R. A., and Ritchie, R. O. (1991). "Fatigue Crack Measurement: Techniques and Applications." L. Engineering Materials Advisory Services, ed., Chameleon, London.
- McCoy, J. J., and Mindlin, R. D. (1963). "Extensional Waves Along the Edge of an Elastic Plate." *Journal of Applied Mechanics*, 30(1), 75-78.
- Miller, G. F., and Pursey, H. (1955). "On the Partition of Energy between Elastic Waves in a Semi-infinite solid." *Proceedings of the Royal Society (London)*, 233(Series A), 55-69.
- Nievergelt, Y. (1999). *Wavelets Made Easy*, Birkhäuser, Boston.
- Ohira, T., and Pao, Y.-H. (1989). "Quantitative Characterization of Microcracking in A533B Steel by Acoustic Emission." *Metallurgical Transactions A*, 20A, 1105-1114.
- Pekeris, C. L. (1955). "The Seismic Surface Pulse." *Proceedings Of the National Academy of Sciences*, 41(7), 469-480.
- Pollack, A. A. (1996). "Acoustic Emission Inspection." *Nondestructive Evaluation and Quality Control*, ASM International, 282-283.
- Proctor, J., Thomas M. (1982). "An Improved Piezoelectric Acoustic Emission Transducer." *Journal of the Acoustical Society of America*, 71(5), 1163-1168.
- Proctor, J., Thomas M. (1986). "More Recent Improvements on the NBS Conical Transducer." *Journal Of Acoustic Emission*, 5(4), 134-142.
- Prosser, W. H., Hamstad, M. A., Gary, J., and O'Gallagher, A. (1999). "Reflections of AE Waves in Finite Plates: Finite Element Modeling and Experimental Measurements." *Journal of Acoustic Emission*, 17(1-2), 37-47.
- Rosmanith, H. P., and Fourney, W. L. (1982). "Determination of Crack-speed History and Tip Locations for Cracks Moving With Nonuniform Velocity." *Experimental Mechanics*, 22(3), 111-116.
- Ruschau, J. J., and Donald, J. K. (1995). "Crack Size Determination." ASTM STP 1251, American Society for Testing and Materials, Philadelphia.
- Scruby, C. B., Baldwin, G. R., and Stacey, K. A. (1985). "Characterization of Fatigue Crack Extension by Quantitative Acoustic Emission." *International Journal of Fracture*, 28(4), 201-222.

- Scruby, C. B., and Buttle, D. J. (1991). "Quantitative Fatigue Crack Measurement by Acoustic Emission." *Fatigue Crack Measurement: Techniques and Applications*, K. J. Marsh, R. A. Smith, and R. O. Ritchie, eds., Chameleon, London, 207-287.
- Thaulow, C., and Burget, W. (1990). "The Emission of Rayleigh Waves from Brittle Fracture Initiation, and the Possible Effect of the Reflected Waves on Crack Arrest." *Fatigue and Fracture of Engineering Materials and Structures*, 13(4), 327-346.
- Theocaris, P. S. (1989). "Elastic Energies Carried with Rayleigh Wave Fronts Determined by Caustics." *Engineering Fracture Mechanics*, 34(3), 709-720.
- Victorov, I. A. (1967). *Rayleigh and Lamb Waves: Physical theory and Applications*, Plenum Press, New York.

Appendix A

Waveforms

This appendix has plots of all the waveforms collected, the resultant signals of the frequency separation, and the spectrum analysis of the low frequency components and wavelet analysis results of selected signals.

The figures of the plotted waveforms and results (as discussed in the section on the data analysis programs) show 2 panels of 4 plots each. The left panel is for channel 1, the right for channel 2. The top plot is the original waveform. The second plot is the low frequency component that is subtracted from the original to get high frequency portion shown in the third plot. The fourth plot is the rectified and thresholded version of the high frequency components. One has to be careful when interpreting the "marker" waveforms in the fourth plot. The height of a spike or indication is the amount above the threshold plus the threshold value, so it is the same amplitude as in the original high frequency component file. The fact that there may be several indications does not mean that each one is an "AE" event. Since most of the data are random excursions, single indications that all have essentially the same amplitude and widely distributed in time, tend to be artifacts from the value of the threshold not being quite high enough. Also one must realize that due to the size of the specimens there is a time window that helps one decide if an event on one channel is the same event on another, a different event or a reflection of the same event. Valid AE events die out over many cycles so typically they manifest as a tight (touching) cluster of indications. Very large events like PLB's die out in approximately 30 msec. The AE is much smaller amplitude so typically they drop to below the noise level in less than 1-2 msec. This is the time it takes for all the reflections to die out. So a larger cluster is most likely a conglomeration of many events and reflections. A longitudinal wave (the fastest) traveling the length of the specimen takes about 8 μ sec. The closest reflection of a longitudinal wave on channel one is from the reflection from the surface of the specimen reflecting again off the crack face at about 10 μ sec. The longest time separation from the same source, is between a surface wave on channel one and longitudinal wave on channel two, and is about 15 μ sec. One cannot distinguish that difference at the scale of these plots. Also, on a single plot, because of the decimation to fit all the data onto the plot it is possible that a cluster of indications ends up as one. It is much better to use the marker files as a guide for where to look, using the Gagescope data acquisition software for the final judgment and ability to save portions of the data in ASCII format for further analysis.

Another type of plot is the spectrum analysis of the low frequency components. Each page has two panels, one for each channel. The original signal and the spectrum are the two plots on each panel.

The last type of figures are wavelet transforms of samples of interesting sections of the high frequency component data. This is a method of analysis that allows the signal to be plotted in time-frequency image where the image contrast/color is a function of the amount of energy (amplitude) available in the signal at a particular time and frequency.

Each blue coded entry in the following tables is a link to the set of plots/panels in another file for that particular condition. One can scroll through the file or click on the page to come back to this appendix. At bottom of the panels are the original filenames of the waveforms being plotted. One can also distinguish what each panel is by knowing the filename nomenclature. The portions of the filename, in order, are:

{Type of steel}
{Type of test: pz for plastic zone or o# for overload #}
{r#, if a repeated run at one of the overload locations}
{0# or ch# for channel # data, # = 1 or 2}.

The filenames can also have sets of prefixes:

LF for Low Frequency component,
HF for High Frequency component,
RT for Rectified and Thresholded version of an HF signal,
WL for wavelet analysis.

The entries are coded so as to increase the amount of information available at a glance. However, one should not make too many conclusions from this information. Even though, in many ways, these tests were conducted in a manner to enhance the ability and chance to capture AE, AE was not monitored for every load the specimens were subjected to, in particular, the precracking. There are some indications in the crack propagation rate data taken during the precracking that point to the possibility of AE occurring in a period of many cycles post-overload rather than during a single overload.

Table A.1 The four-panel plots

	Steel Type (in order of increasing yield strength)						
Test ↓	A36	1018	A588	HPS70	A514	A2, R50	A2, R60
Plastic Zone	ACB	AC2	AC2	#0	AC2		
Overload 1	#S	#0	#0	#S	#S	#S	#S
Overload 2	#0	#0	#0	#S	#S	#S	FB #L
Overload 3	#0	#0	#0	#0	#S	FB #L	
Overload 4	#0	#0	#0	#0	#S		
Overload 5	#0	#0	#0	#S	#0		
Overload 6	#S	#0	#0	#0	#S		
Overload 7	#0	#0	#0	#S	#0		
Overload 8	#S	#0	#0	#S	#0		
Overload 9	#S	#0	#0	#0	#S		
Overload 10	FP #L	FP #S	#0	#0	#0		
Overload 11			FP #0	#0	#S		
Overload 12				FP #S	#0		
Overload 13					#S		
Overload 14					#0		
<p>Code legend: FP = Failure by Plastic Hinge FB = Failure by Brittle Fracture #0 = No AE in high frequency (HF) component #S = small number of events, less than 20 #L = large number of events, typically much greater than 20 ACB = AE both channels, AC2 = AE channel 2 only</p>							

Table A.2 The low frequency component spectrum plots

	Steel Type (in order of increasing yield strength)						
Test ↓	A36	1018	A588	HPS70	A514	A2, R50	A2, R60
Plastic Zone	ACB	AC2	AC2	#0	AC2		
Overload 1	#S	#0	#0	#S	#S	#S	#S
Overload 2	#0	#0	#0	#S	#S	#S	FB #L
Overload 3	#0	#0	#0	#0	#S	FB #L	
Overload 4	#0	#0	#0	#0	#S		
Overload 5	#0	#0	#0	#S	#0		
Overload 6	#S	#0	#0	#0	#S		
Overload 7	#0	#0	#0	#S	#0		
Overload 8	#S	#0	#0	#S	#0		
Overload 9	#S	#0	#0	#0	#S		
Overload 10	FP #L	FP #S	#0	#0	#0		
Overload 11			FP #0	#0	#S		
Overload 12				FP #S	#0		
Overload 13					#S		
Overload 14					#0		
<p>Code legend: FP = Failure by Plastic Hinge FB = Failure by Brittle Fracture #0 = No AE in high frequency (HF) component #S = small number of events, less than 20 #L = large number of events, typically much greater than 20 ACB = AE both channels, AC2 = AE channel 2 only</p>							

Table A.3 The wavelet analyses

	Steel Type (in order of increasing yield strength)						
Test ↓	A36	1018	A588	HPS70	A514	A2, R50	A2, R60
Plastic Zone	ACB	AC2	AC2		AC2		
Overload 1				#3S	#2S	#4S	#4S
Overload 2				#4S	#1S	#4S	FB #4L
Overload 3					#4S	FB #5L	
Overload 4					#1S		
Overload 5				#1S			
Overload 6	#2S				#1S		
Overload 7			#1?	#1S			
Overload 8	#6S			#2S			
Overload 9	#8S				#4S		
Overload 10	FP #8L	FP #1S					
Overload 11			FP #0		#2S		
Overload 12				FP #1S			
Overload 13					#3S		
Overload 14							
<p>Code legend: FP = Failure by Plastic Hinge FB = Failure by Brittle Fracture #0 = No AE in high frequency (HF) component #nS = n HF events analyzed, typically all the possible events in that test #nL = n sample of HF events analyzed from a large group (>>20) ACB = AE both channels, AC2 = AE channel 2 only</p>							

Appendix B

Data Analysis Programs

This appendix has the complete documentation of the data analysis programs used in this dissertation. These programs were written in LabView, a visual dataflow paradigm, hence the code is a collection of schematic-like images. Each name is a link to the print document.

Main programs (VI's in LabView parlance)

[ViewSpectSig.VI](#)

[ViewPeakDetectSig.VI](#)

Sub Programs (SubVI's in LabView parlance)

[BoxcarFilterSub.VI](#)

[MyReadGageSigSub.VI](#)

[MySampleGageSigNoiseSub.VI](#)

[MyWriteSigwFilenameSub.VI](#)

[RectifyandThresholdSub.VI](#)

[SmartZeroPadderSub.VI](#)

Tools

[peekbyte.VI](#)

[peekword.VI](#)

Appendix C

Micrographs

This appendix presents the complete set of micrographs for all the tests. Each blue entry in the table below is a link to other files with the set of micrographs for different types of images for a particular specimen condition. One can scroll through the pictures but clicking anywhere on a page links back to the table. Most of the sets have pictures for both before and after the overload.

There are several sets of micrographs per page, each set a different magnification. The specimen orientation for most sets is crack horizontal, entering from the left. The vertical lines are scribe marks 0.050 inches apart. The low magnification sets are oriented; crack vertical entering from top. Some sets are of other areas of a specimen, if there is extensive deformation.

The "flat" images are straight micrographs that do not use any technique to enhance contrast with topographic information. The "topographic" images were created using one of two methods for creating contrast from surface topography; differential interference contrast (DIC) and an ad-hoc brightfield technique. The DIC method or Nomarski as it is sometimes called, uses polarized light passing through a Nomarski-modified Wollaston (double quartz birefringent) prism which splits the light into two images, one sheared (lateral shift) slightly, but less than the resolving power of the objective. Surface topography of the specimen creates slight variations in path length for corresponding rays in each image so that when the two images are recombined interference creates contrast in the image. The other technique is an ad-hoc brightfield technique using a stereo microscope because of its low magnification and large distance above the stage. In the later overloads where the surface topography became so great (normal to the specimen) or covered such a large area, the DIC mode was inadequate due to lack of depth of field or field of view. It was discovered that if the light from a large diffuse distant source, in this case, the fluorescent ceiling lights, was reflected off the specimen into the microscope by tilting the specimen, the topography could be enhanced because some areas would reflect light away from the optical axis while others reflect into the axis hence creating image contrast. This was better than oblique lighting or any dye and wipe technique (where the surface is colored and the high regions wiped clean) because it shows local texture even though the entire region might be below the original plane of the surface, such as is crack tip deformation.

Table C.1 Micrographs

	Steel Type (in order of increasing yield strength)						
Test ↓	A36	1018	A588	HPS70	A514	A2, R50	A2, R60
Plastic Zone	V F T	V F T	V F T	V F T	V F T		
Overload 1	F T	F T	F T	F T	F T	F T	F T
Overload 2	F T	F T	F T	F T	F T	F T	F T
Overload 3	F T	F T	F T	F T	F T	F T	
Overload 4	F T	F T	F T	F T	F T		
Overload 5	F T	F T	F T	F T	F T		
Overload 6	F T	F T	F T	F T	F T		
Overload 7	F T	F T	F T	F T	F T		
Overload 8	F T	F T	F T	F T	F T		
Overload 9	F T	F T	F T	F T	F T		
Overload 10	F T	F T	F T	F T	F T		
Overload 11			F T	F T	F T		
Overload 12				T	T		
Overload 13					T		
Overload 14					T		
<p>Code legend: V = virgin, pre-1 Kip preload, has both flat and topographic images F = flat microscopy, no topography enhancement technique T = topographic image contrast</p>							

Vita

Michael R. Horne was born September 28, 1958 in the United States. He graduated from Boonsboro High School, Boonsboro, Maryland in 1976, while concurrently taking classes at Hagerstown Junior College, Hagerstown, Maryland. Upon graduation from the Engineering Transfer curriculum at the Junior College with an Associate of Arts Degree in 1978, he transferred to the Department of Engineering Science and Mechanics at Virginia Tech in Blacksburg, Virginia. He graduated with a Bachelor of Science Degree in 1980. Between his graduation and his return in 1985 to V.P.I. to work on a Master of Science Degree in Engineering Mechanics, he worked as a research engineer at Arctec, Inc. in Columbia, Maryland, an Engineering Computer Support engineer at Grove Manufacturing, Shady Grove, Pennsylvania and as a part-time instructor in Engineering at Hagerstown Junior College. For a period of his tenure as a Master's candidate he was a NASA Fellow in the Materials Characterization and Instrumentation Section, Langley Research Center in Hampton, Virginia. Upon completion of his M.S. degree he remained at Virginia Tech to work on a Ph.D. in Materials Engineering Science. During this period he also worked in the capacity of instructor and research staff.